

**POTENTIAL NEGATIVE EFFECTS OF WIND TURBINES
ON THE EAR**

A Thesis
Presented to
The Academic Faculty

by

Rolan S. Duvvury

In Partial Fulfillment
of the Requirements for the Degree
Master of Science in the
School of Civil and Environmental Engineering

Georgia Institute of Technology
August 2011

POTENTIAL NEGATIVE EFFECTS OF WIND TURBINES ON THE EAR

Approved by:

Dr. Mulalo Doyoyo, Advisor
School of Civil and Environmental Engineering
Georgia Institute of Technology

Dr. Leroy Z. Emkin
School of Civil and Environmental Engineering
Georgia Institute of Technology

Dr. Arash Yavari
School of Civil and Environmental Engineering
Georgia Institute of Technology

Dr. Abdul-Hamid Zureick
School of Civil and Environmental Engineering
Georgia Institute of Technology

Date Approved: 7/11/2011

To my parents, for without their continuous support and guidance I would not be here today.

ACKNOWLEDGEMENTS

First and foremost, I would like to thank my advisor, Dr. Doyoyo for all his guidance, encouragement, support, and inspiration during the research beginning when I was an undergraduate student. I will never forget our endless yet stimulating discussions about science, engineering, and other topics of life. I would also like to thank the faculty of both the School of Architecture and the School of Civil and Environmental Engineering with whom it was an honor and a pleasure to learn from during my time here at Georgia Tech. I am grateful to Dr. Emkin, Dr. Yavari, and Dr. Zureick for agreeing to be a part of my thesis committee. Finally, I wish to thank my parents who always had confidence in me and gave me continuous support and guidance throughout.

TABLE OF CONTENTS

	Page
ACKNOWLEDGEMENTS	iv
LIST OF TABLES	vii
LIST OF FIGURES	viii
SUMMARY	xi
<u>CHAPTER</u>	
1 INTRODUCTION	1
Current Wind Turbine Technology	1
Measuring Wind Turbine Noise on the Ear	2
2 WIND TURBINE NOISE EFFECTS ON THE EAR	6
Chapter Overview	6
Sound Propagation from a Point Source	7
A Wind Farm as a Point Source	8
Properties of the Tectorial Membrane	11
Stress-Strain Relationship of the Tectorial Membrane	15
Damage of the Tectorial Membrane	18
3 NEXT-GENERATION AUTONOMOUS HOUSING	31
Chapter Overview	31
The Autonomous House	32
Cost-Modeling the Autonomous House	33
Principles of Cube Symmetry and Modular Design	34
Design of the L-module – Use of the Cube	37

Design of the “Beehive” Structure – Zulu Design, Shells, and Rotational Symmetry	40
Design of the Village – Zulu Layout and Group Symmetry	46
Final Design of the Village	50
Wind Farm Specifications	51
Suggested Distances between the Wind Farm and the Autonomous Village	52
REFERENCES	53

LIST OF TABLES

	Page
Table 1: Strain energy due to the number of cycles of applied osmotic pressure.	23
Table 2: Damage parameter D of the tectorial membrane vs. distance d away from a wind farm point source for transverse z -axis displacements δ_z between 10 and 100 μm .	29

LIST OF FIGURES

Figure 1: Illustration of IEC 61400-11 schematic for acoustic emission measurement.	Page 4
Figure 2: Unweighted wind turbine noise spectra taken from van den Berg (2006) and Jung et al. (2008) for frequencies between 1 and 1000 Hz.	5
Figure 3: Sound propagation from a point source at distances r_1 and r_2 .	7
Figure 4: Global map of average wind speeds at 80m (Archer and Jacobson 2005).	9
Figure 5: Total A-weighted sound pressure level L_p vs. distance r in log scale.	10
Figure 6: <i>In-situ</i> tectorial membrane segment overlaying the organ of Corti.	12
Figure 7: Plot of stress-strain curve of the apical-middle region of the tectorial membrane using constants $a = 0.31$ and $b = 0.31$ from Masaki et al. (2006).	16
Figure 8: Tensile stress-strain curves for four natural rubber compounds of different hardnesses (adapted from Lindley 1966).	17
Figure 9: Video-enhanced DIC images of the tectorial membrane taken from Cotanche (1992).	19
Figure 10: SEM micrographs of rubber of two different specimens taken from Wang et al. (2002).	20
Figure 11: Hysteresis loops for the tectorial membrane when subjected to cycles of osmotic pressure.	21
Figure 12: Hysteresis loops for a purely viscoelastic computation of rubber damage when subjected to cyclic tension.	21
Figure 13: The tectorial membrane modeled as a simply-supported beam of length l , width w , and thickness t with an external force P_{ext} from a wind farm applied at midspan.	24
Figure 14: Damage of the tectorial membrane vs. the z-axis displacement.	26
Figure 15: Damage of the tectorial membrane based on unweighted decibel values in the infrasound range vs. z-axis displacement at a distance $d=500\text{m}$ from a wind farm.	27

Figure 16: Damage parameter D of the tectorial membrane vs. distance d (m) for displacements δ_z between 10 and 100 μm .	30
Figure 17: Current examples of autonomous housing.	32
Figure 18: Example of process-based cost model methodology.	33
Figure 19: Three classes of the ninety-eight cube configurations (Economou and Baker 2006).	35
Figure 20: Exploded axonometric (1), plans (2), and stacking model (3) of the module cubes in Habitat '67 (Canadian Architecture Collection, McGill University 2001).	36
Figure 21: Axonometric (1), plan (2), and stacking arrangement (3) of the prefab modular capsule in Nakagin Tower (Kurokawa 1977; Schmal et al. 2005; Ross 1978).	37
Figure 22: 3D model of the L-module (generated in Autodesk 3ds Max).	38
Figure 23: Plan and section cuts of the L-module.	38
Figure 24: (1) Section cut of modules being stacked with (2) elevation of façade; (3) detail of shear release.	39
Figure 25: Modules being locked into “core” structure (generated in Autocad 3ds Max).	39
Figure 26: Examples of Zulu beehive dwellings.	40
Figure 27: (1) Ribbed reinforced concrete shell and (2) shell braced by concrete “Y” flying buttresses in the Palazzetto dello sport.	41
Figure 28: The two planar point groups: cyclic (C_n) and dihedral (D_n) (Steadman and March 1971).	42
Figure 29: Examples of point groups in architectural plans (Steadman and March 1971).	43
Figure 30: A typical floor plan of the beehive commune.	44
Figure 31: Complete structural model (generated in Rhinoceros 3D).	44
Figure 32: Module arrangement within the building (generated in Rhinoceros 3D).	45
Figure 33: Complete view of the beehive commune (generated in Rhinoceros 3D).	45

Figure 34: Layout of the Zulu Royal Settlement – Mgungundlovu (Kuper 1993).	46
Figure 35: Layout of a Zulu homestead (Kuper 1993).	47
Figure 36: Wallpaper W_6^I with six point rotations and one direct translation (Steadman and March 1971).	48
Figure 37: Overlay of hexagonal tiling of beehive communes on the W_6^I wallpaper configuration.	49
Figure 38: Final layout of the proposed village.	51

SUMMARY

This thesis presents investigations on the potential negative effects of wind turbine noise on the human ear from a sound point source (i.e. wind farm). In Chapter 2, the tectorial membrane, which is a crucial gelatinous structural matrix located within the cochlea of the inner ear, is considered to have a similar constitutive stress-strain relationship to that of an elastomer (rubber) in tension. The tectorial membrane appears to stretch when subjected to constant heavy sound stimulation. The tectorial membrane is modeled as a simply-supported beam with an external load P_{ext} applied at midspan. A virtual work approach is used to balance the external work at midspan $P_{ext}\delta_z$ of the tectorial membrane with the internal strain energy $U(\varepsilon_z)$ from its hysteresis loops. These hysteresis loops quantify the amount of damage that the tectorial membrane undergoes due to an applied external loading. Normalized damage tables are presented at the end of the chapter to suggest safe distances away from the wind turbines to limit damage to the tectorial membrane. Chapter 3 considers a hypothetical autonomous village constructed in South Pretoria, South Africa. This village accommodates approximately 2000 people (~500 families) and receives electricity for hot water from a nearby 2.5 MW wind farm. The design process for the village is discussed from an architectural and design standpoint. The wind farm specifications, specifically the number of 2.5 MW wind turbines needed to provide electricity for hot water, are established. Results from Chapter 2 are used to suggest minimum safe distances between the wind farm and the autonomous village in the context of limiting damage to the tectorial membrane.

CHAPTER 1

INTRODUCTION

Current Wind Turbine Technology

Recently, wind turbine technology has gathered worldwide attention because of the need to foster renewable energy infrastructure across the globe. Many investigations on wind turbines focus exclusively on current and future power output potential and efficient ways to harness this energy. Modern land-based wind turbines can individually produce power generally between 1.5 MW and 2.5 MW. Offshore wind turbines are larger and are rated around 4.0 MW, but prototypes for 5 MW offshore wind turbines are already being developed (Archer and Jacobson 2005; Musial et al. 2006; Thresher et al. 2008; Martínez et al. 2008; Lu et al. 2009).

A typical coal-fired plant can currently produce net power of around 500 MW. Coal-based plants that are under 35 years old have an average capacity of about 550 MW (Bohm et al. 2007; MIT 2007; Beér 2009). World coal consumption is expected to increase by 65% in the next 20 years (EIA 2008). Thus, it might appear as though wind turbines will be maintained in the future as a supplementary energy source. However, if the push for increased development of wind technology occurs, there will be other issues to consider besides improving power output capacity and exploiting energy efficiently. While coal burning has numerous environmental and health hazards such as air and water quality disturbance (Greb et al. 2006), wind turbines produce constant noise that could be harmful to the human ear over time. Various ontological symptoms such as tinnitus and

aural pain and pressure have been reported by residents who reside near wind turbines (Salt and Hullar 2010).

Measuring Wind Turbine Noise on the Ear

It is well known that sustained exposure to noise can cause temporary threshold shifts (TTS) and depending on the level and duration can result in long-term auditory fatigue. According to Charron and Botte (1988), sounds greater than 85 decibels are characterized as high-level stimuli and can result in long-term ear fatigue. A modern wind farm consisting of multiple turbines can emit sound power levels between 94 and 103 A-weighted decibels (dBA) for wind speeds between 5 and 10 m/s, respectively (van den Berg 2003). Acoustic noise is generally recorded using A-weighted decibels that account for human hearing sensitivity from the unweighted wind turbine noise spectrum data. At distances no greater than 500m and/or located within rural settings, a wind turbine farm can generate perceivable sound levels generally between 30 and 50 dBA. These values are calculated for land-based wind turbines (between 1.5 MW and 2.5 MW) functioning during the day and night with average wind speeds of around 8 m/s (Keith et al. 2008; Pederson et al. 2009; Salt and Hullar 2010).

Since wind turbine sound levels at significant distances fall well below the critical threshold for human hearing loss from sustained exposure (~90-105 dBA), they have been deemed safe for the ear by many previous studies, including BWEA (2000) and Colby et al. (2009). But this does not account for the complexity of the ear and its response to low frequency sounds. Low frequency sounds that fall below the range of the normal audible range of 20 Hz and 20 kHz are collectively known as infrasound. Wind

turbines generate infrasound at frequencies and levels not necessarily perceived by the human ear, which may result in long term damage (Salt and Hullar 2010). This suggests that there is the possibility that the constant sound generated from multiple wind turbines, even at a lower frequency, can cause auditory fatigue and cumulative damage to the ear over years of exposure.

There are currently two major sound measurement procedures that are used for determining decibel levels from wind turbines. The first standard is IEC 61400-11 which is published by the International Electrotechnical Committee (IEC) and addresses acoustic noise from wind turbines. The second standard is ISO 7196 which is published by the International Organization for Standardization (ISO) and specifies a frequency-weighted characteristic (G) for determining weighted sound pressure levels that are deemed as infrasound. The former code reports A-weighted sound power levels, 1/3 octave levels, and tonality at wind speeds between 6-10 m/s (IEC 2002; Huskey 2006; Jung et al. 2008). The IEC 61400-11 procedure generally records perceptible wind turbine noise as ~30-50 dBA. Figure 1 illustrates the method used by IEC 61400-11 for measuring acoustic emission.

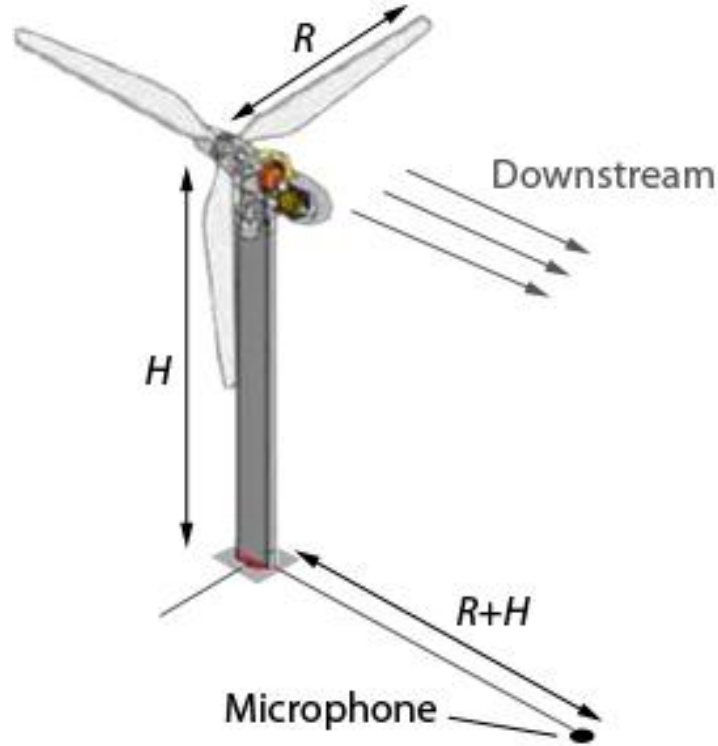


Figure 1. Illustration of IEC 61400-11 schematic for acoustic emission measurement. A microphone is placed in the downstream direction at a distance, $R+H$ away from a wind turbine of hub height, H and rotor radius, R . Image derived from Jung et al. (2008).

Jung et al. (2008) reported that, a 1.5 MW wind turbine generates a direct relationship between wind speed and sound pressure level. At an $R+H$ distance of 98m, where R is the rotor radius and H is the hub height, sound pressure levels range between ~54 and ~65 dBA for wind speeds between ~7 and ~14 m/s, respectively. Additionally, a comparison of sound spectral densities revealed that low-frequency acoustic waves including infrasound decayed more slowly and covered a wider range of dB levels (~100 dBA to ~55 dBA) than high-frequency ones. Data collected using the ISO 7196 standard reported similar results to those using the IEC 61400-11 code.

Figure 2 depicts the unweighted wind turbine noise spectrum recorded by van den Berg (2006) and Jung et al. (2008) for frequencies between 1 and 1000 Hz. The

infrasound range is marked in the figure (<20 Hz). At ~ 700 Hz, the A-weighted sound pressure level is ~ 40 dBA. Conversely, at ~ 3 Hz, the unweighted sound pressure level generated by the wind turbine is ~ 80 dB.

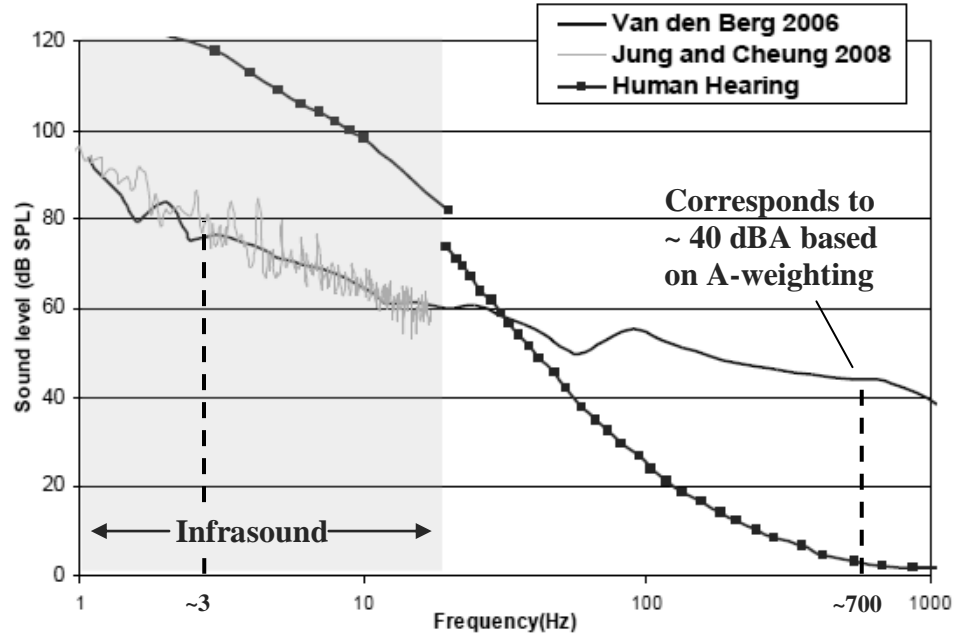


Figure 2. Unweighted wind turbine noise spectra taken from van den Berg (2006) and Jung et al. (2008) for frequencies between 1 and 1000 Hz. Adapted from Salt (2010).

CHAPTER 2

WIND TURBINE NOISE EFFECTS ON THE EAR

Chapter Overview

This chapter is concerned with about the effects of wind turbine noise on the ear, particularly the tectorial membrane, and a potential method to quantify the damage. The first part of this chapter is about the relationship of how sound pressure levels vary with distance due to sound propagation from a point source and how wind turbines can be modeled as these point sources. The theory of noise propagation from a point source is first established to set the context for its application to a wind farm. Using the wind farm model given by van den Berg (2003) as a point source, the sound pressure levels are then calculated at distances of up to 500 m away. In the next part of this chapter, the mechanical properties of the tectorial membrane, a gelatinous structural matrix within the cochlea of the inner ear that is critical for hearing, are discussed in detail. The tectorial membrane appears to demonstrate non-linear behavior throughout a majority of its stress-strain curve and seems to resemble a general stress-strain curve of an elastomer (rubber) in tension. Due to this nonlinearity, the constitutive stress-strain relationship of the tectorial membrane is established through a power law. In the final part of this chapter the damage from sound pressure levels on the tectorial membrane are investigated. The tectorial membrane appears to partially stretch when exposed to sustained loud noise. The tectorial membrane is modeled as a simply supported beam loaded at midspan, and Castigliano's first theorem (virtual work) and rubber damage modeling methods are used as ways to quantify the damage due to sound pressure levels from wind turbines.

Sound Propagation from a Point Source

In order to discuss how sound pressure levels vary with distance, it is necessary to first understand how noise propagates through a medium from a point source. Under ideal conditions, sound from a point source propagates waves equally in all directions (spherical spreading) and follows the Inverse-square law. Each time the distance doubles away from the source, the sound level drops by 6 dB (Lamancusa 2009; Traux 1999). At distances r_1 and r_2 away from a point source, where r_2 is twice the distance of r_1 , their decibel difference DD can be expressed by:

$$DD = 20 \log(r_1 / r_2) \quad (1)$$

A diagram based on the Inverse-square law of sound propagation radiating from a point source at distances r_1 and r_2 is shown in figure 3.

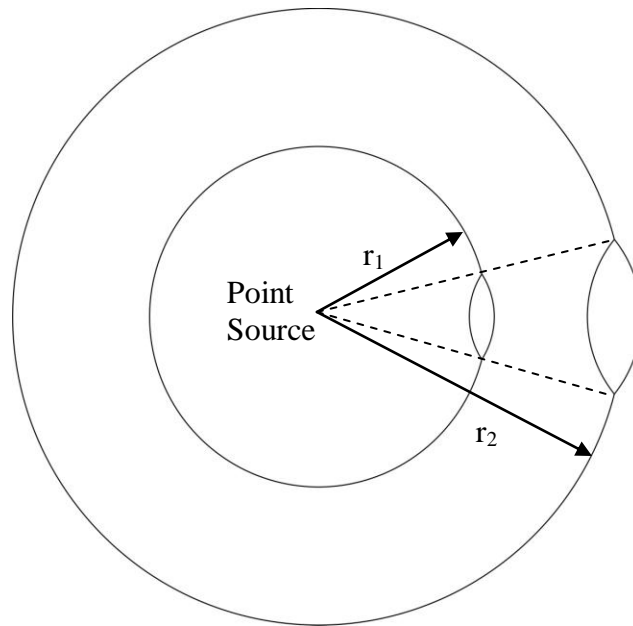


Figure 3. Sound propagation from a point source at distances r_1 and r_2 . At distance r_2 , which is twice the distance of r_1 , the sound level drops by 6 dB.

A point source whose dimension is small as compared to its sound wavelength radiates sound waves in an omni-directional pattern, while a point source that is relatively large compared to its sound wavelength radiates these waves directionally. Thus, a directivity factor, Q and directivity index, DI can be expressed with the following equations:

$$Q = \frac{P_{\theta}^2}{P_s^2} \quad DI = 10 \log_{10} Q \quad (2, 3)$$

where, P_{θ} refers to sound pressure for a directional source and P_s is the sound pressure of a non-directional point source. The total sound power level, L_p (in dB) of a single source propagating in an atmosphere can be represented by the following equation:

$$L_p = L_w - 20 \log r - 11 + DI - A_{abs} - A_E \quad (4)$$

where, L_w is the sound power level of the source, r is the distance away from the point source, A_{abs} is the atmospheric absorption factor, and A_E is the excess attenuation factor. This excess attenuation factor, A_E can be calculated as the sum of various terms:

$$A_E = A_{ground} + A_{weather} + A_{vegetation} + A_{turbulence} + \dots \quad (5)$$

where, A_{ground} is the attenuation due to the ground and terrain interaction, $A_{weather}$ is the attenuation due to meteorological effects, $A_{vegetation}$ is the attenuation due to forests and trees, $A_{turbulence}$ is the attenuation due to atmospheric turbulence (Lamancusa 2009). Other effects can also be added to the equation to determine a final A_E value.

A Wind Farm as a Point Source

Recent studies have suggested that a wind turbine of hub height h can be modeled as a point source in terms of noise propagation originating from the turbine blades

(Makarewicz 2011). Thus, the total A-weighted sound pressure level of a point source, L_p (in dBA) can be expressed by the following equation:

$$L_p = L_w + 10 \log \left\{ \frac{r_0^2}{2\pi r^2} 10^{-0.0005r} \right\} \quad (6)$$

where, L_w is the initial A-weighted sound power level (in dBA), r is the distance away from the point source, r_0 is the initial distance, and the excess attenuation factor A_E which includes all frequency contributions) is assumed to be 0.005 (Makarewicz 2011).

In order to model the effects of a wind farm as a point source, it is first necessary to establish its decibel level production. As given in van den Berg (2003) and mentioned in Chapter 1, the initial sound power level L_w of the wind farm studied varied between 94 and 103 dBA for wind speeds between 5 and 10 m/s, respectively. From Archer and Jacobson (2005), the average global wind speed at a height of 80 m is ≥ 6.9 m/s. Although this value falls between the numbers from van den Berg (2003), the maximum of 10 m/s will be assumed as the wind speed. Figure 4 depicts a global map of average wind speeds at a height of 80 m taken from Archer and Jacobson (2005).

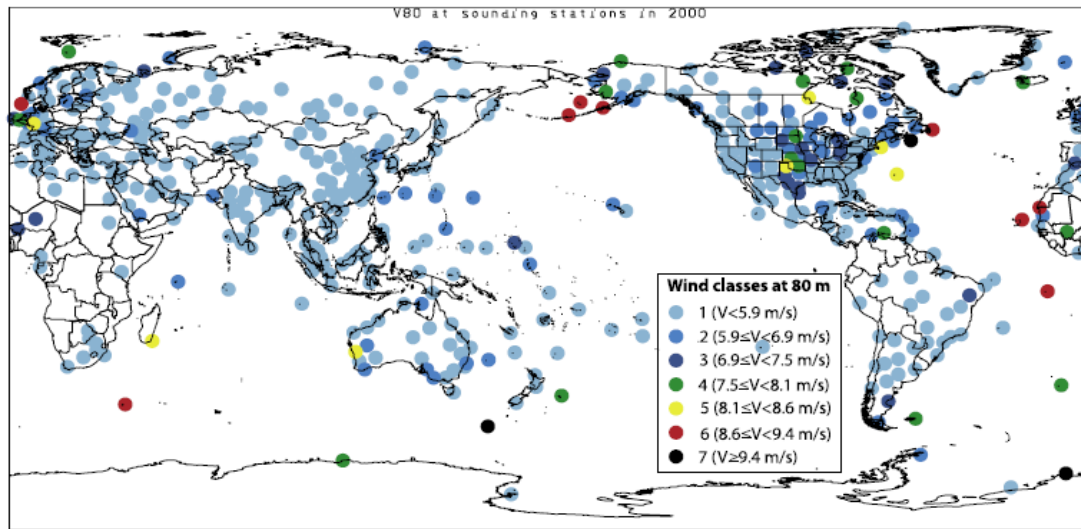


Figure 4. Global map of average wind speeds at 80 m. (Archer and Jacobson 2005).

A wind speed of 10 m/s corresponds directly to 103 dBA for the wind farm data provided in van den Berg (2003). Thus, at a height of 80 m (assumed hub height h) the wind farm generates an initial L_w of 103 dBA. Using this wind farm sound pressure level data as a point source and the equation provided from Makarewicz (2011), a plot of the total A-weighted sound pressure levels of the wind farm versus distance is presented starting with an initial L_w value of 103 dBA (figure 5).

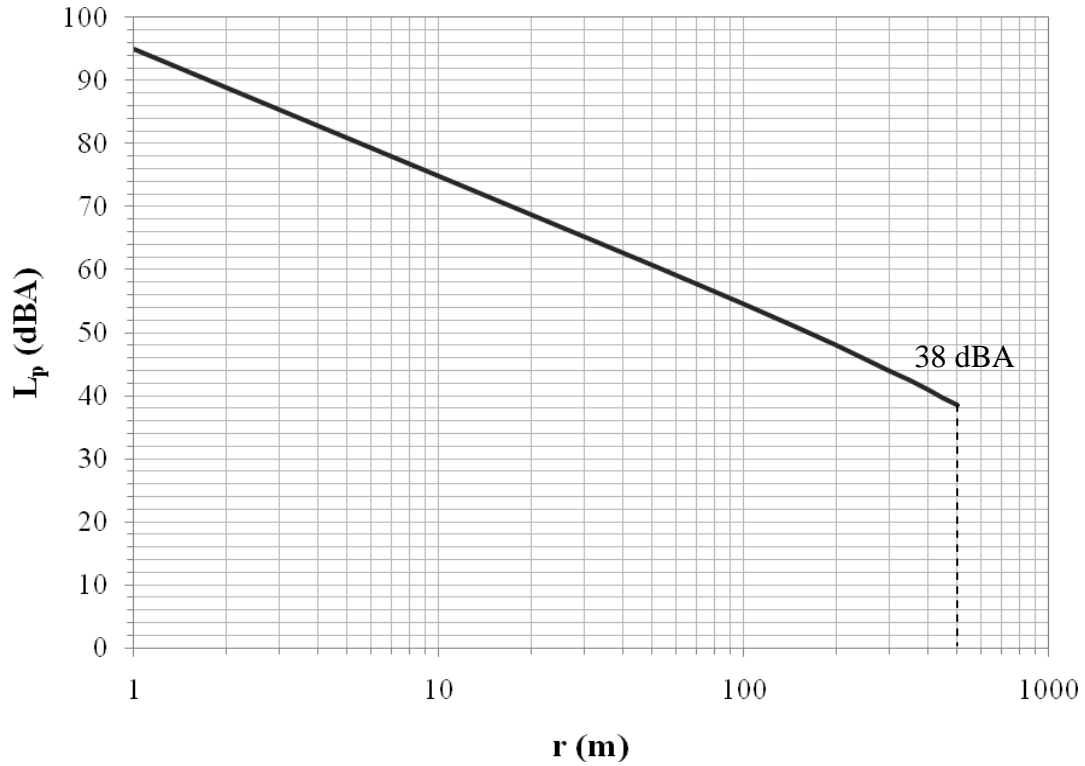


Figure 5. Total A-weighted sound pressure level (L_p) vs. distance (r) in log scale.

From figure 5, it can be seen that at a distance $d=500\text{m}$ away from the wind farm, the perceivable sound pressure level is 38 dBA. As all the values in figure 5 are A-weighted sound pressure levels, they have been adjusted due to human hearing sensitivity. From Salt (2010), the wind turbine noise spectra curve at $\sim 40\text{ dB}$ corresponds to an A-weighted value of $\sim 40\text{ dBA}$ at $\sim 700\text{ Hz}$, as marked in figure 2. This is

perceivable as it is clearly above the upper limit for infrasound (20 Hz). On this same curve, a sound pressure level of ~80 dB (unweighted) generated by the wind turbine farm is off of the A-weighting scale and corresponds to an extremely low frequency of ~3 Hz (infrasound). At ~3 Hz, there is nearly a 120 dB difference between the actual sound pressure level (~80 dB) and the A-weighted sound pressure level (~ -40 dBA).

Properties of the Tectorial Membrane

As mentioned in the chapter overview, the tectorial membrane is a gelatinous structural matrix that is within the cochlea of the inner ear. It contains 97% water as well as macromolecular polyelectrolytes. It overlays the hair cell bundles of the organ of Corti (figure 6) and, although previously overlooked in past research, is currently thought to play a crucial role in cochlear mechanics, particularly with regards to stimulating the hair cells. From Gueta et al. (2006), the tectorial membrane spans the length of the cochlea and its approximate dimensions are ~100 μm and ~50 μm in the radial (x) and transverse (z) directions, respectively. Thus, the cross-sectional area normal to the x-z plane is approximately 5000 μm^2 . Although it spans the entire cochlear length, the tectorial membrane is cut into longitudinal segments ~500-1000 μm for testing. The area normal to the x-y plane ranges between 5×10^4 and $1 \times 10^5 \mu\text{m}^2$ (Ghaffari et al. 2010).

Structurally, the tectorial membrane is made up of two major components: collagen fibrils and non-collagenous proteins. There are also multiple proteins within the tectorial membrane including α -tectorin, β -tectorin, and collagen type XI, and any genetic modification of them could lead to significant hearing loss. The glycoprotein β -tectorin is a necessary structural component and provides non-negligible longitudinal coupling in

the tectorial membrane. Additionally, the tectorial membrane is very important in sensitivity and frequency selectivity in the inner ear (Masaki et al. 2006, Ghaffari et al. 2007; Richter et al. 2007; Gu et al. 2008).

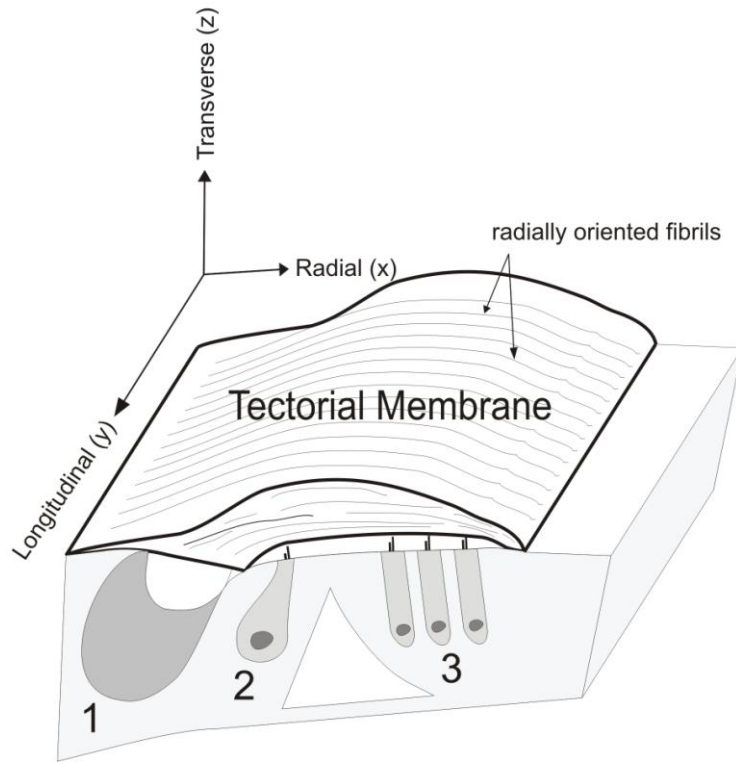


Figure 6. *In-situ* tectorial membrane segment overlaying the organ of Corti. (1) spiral limbus; (2) outer hair cells; (3) inner hair cells.

Although initially thought to have uniform mechanical stiffness and originally rendered as an isotropic homogenous rigid plate, research has shown that the tectorial membrane has important anisotropic mechanical properties with increased stiffness (mechanical impedance) in the radial direction. This is due to the fact that the collagen fibrils are organized as thick fibers ($\sim 1 \mu\text{m}$) and are radially oriented in the tectorial membrane (figure 6). Additionally, these collagen fibers have been shown to be thicker and closer together at the base of the tectorial membrane than at the apex. Furthermore, they are embedded within a tectorin based striated-sheet matrix. The tectorial membrane

has also been modeled as a resonant system acting in the transverse direction, but no current observations have confirmed the theory of tectorial membrane resonance. It seems that the mammalian inner ear is dependent on this anisotropic matrix in guiding sound-induced vibrations to specific sensory hair cells in the organ of Corti. In addition to its anisotropy, the tectorial membrane also displays viscoelastic properties. The frequency dependence of the displacement of the tectorial membrane can be characterized somewhere between pure viscosity (i.e. viscous damper) and pure elasticity (i.e. linear spring), meaning that both are relevant. Results show that the viscoelastic properties of the tectorial membrane extend over a wide range of audio frequencies. (Davis 1965; Geisler and Sang 1995; Abnet and Freeman 2000; Richter et al. 2007; Gu et al. 2008; Richardson et al. 2008; Gavara and Chadwick 2009; Lukashkin et al. 2010; Meaud and Grosh 2010).

Based on results computed by Richter et al. (2007), the transversal stiffness of the tectorial membrane taken at five different locations ranged between 0.005 N/m and 0.166 N/m. The radial stiffness at these five locations ranged between 0.007 N/m and 0.288 N/m. Longitudinal stiffness was calculated to be around 0.15 N/m. From Gu et al. (2008), it was found that the effective stiffness of the tectorial membrane increased with frequency. Additionally, the shear stiffness of the tectorial membrane was reported to be about 3-6 N/m and increased with frequency. As this value is much higher than the stiffness values of the hair cell bundles (0.25 N/m), it is unlikely that they would have much effect on shearing the tectorial membrane and would most likely move with it (bulk motion).

Different studies have revealed that the tectorial membrane has a larger Young's modulus (E) at the base than at the apex. A recent study done by Gavara and Chadwick (2009) found the Young's modulus to be around 1.93 kPa and 0.78 kPa at the base and apex, respectively. Richter et al. (2007) reported similar values for Young's modulus of the tectorial membrane at around 1.9 kPa at the base and 0.53 kPa at the apex. According to Shoelson et al. (2004), the Young's modulus was uniform for both the base and the apex of the tectorial membrane of ~4.5 kPa. Gueta et al. (2006) reported grossly higher values of 215 kPa and ~25 kPa at the base and apex, respectively. Of all of these experiments, the study by Richter et al. (2007) was the only one done *in situ* and appears to be most consistent with Gavara and Chadwick (2009). The latter group speculates the reason for the large discrepancy from data of Gueta et al. (2006) might be because of the small size of their probe which can overestimate the Young's modulus.

From a more recent study done by Gueta et al. (2008), Atomic Force Microscopy (AFM) and finite element modeling were used to find the Young's modulus in the principal orthogonal directions (x, y, and z). The study revealed that the Young's modulus of the tectorial membrane in the apical, midturn, and basal regions was 11 kPa, 18 kPa, and 45 kPa, respectively in the radial (x) direction. In the longitudinal (y) direction, Gueta et al. (2008) reported values of 16 kPa, 31 kPa, and 75 kPa, for the apical, midturn, and basal regions, respectively. With regards to the transverse (z) direction, the reported values from Gueta et al. (2008) were 28 kPa, 73 kPa, and 300 kPa in the apical, midturn, and basal regions, respectively. Gavara and Chadwick (2009) maintain that the study done by Gueta et al. (2008) along the orthogonal directions does

not correctly represent the anisotropic model of the tectorial membrane, and thus reports inaccurate modulus values.

Finally, shear modulus calculations of the tectorial membrane also varied widely between studies. In Richter et al. (2007), the shear modulus was found to be ranging between 0.1-1.2 kPa. Shoelson et al. (2004) found the shear modulus between 1.2-8.6 kPa. In the study done by Gu et al. (2008), the shear modulus was determined to be significantly larger ranging between 17-50 kPa.

Stress-Strain Relationship of the Tectorial Membrane

In order to determine the potential effects of wind turbine noise on the tectorial membrane, it is first necessary to establish its constitutive stress-strain relationship. From Masaki et al. (2006), the tectorial membrane of a mouse was submerged in a bathing solution. Polyethylene glycol solutions with a molecular mass between 20 and 511 kDa were added to this bathing solution to exert osmotic pressure in the range of 0.025-10 kPa on the tectorial membrane. They found that the tectorial membrane shrank in size with an increase in osmotic pressure. Thus, the stress-strain relationship of the tectorial membrane was determined to be generally non-linear and was related by the power function:

$$\varepsilon_z = a\sigma_c^b \quad (7)$$

where, σ_c is the applied stress, ε_z is the strain in the -z direction as a function of the applied stress, and a and b are constants used for fitting the power curve. With algebraic manipulation, the equation for the applied stress as a function of the strain can be rewritten from Eq. (7) using the preceding defined variables:

$$\sigma_c(\varepsilon_z) = \left(\frac{\varepsilon_z}{a} \right)^{\frac{1}{b}} \quad (8)$$

Using Eq. (8) and constants $a = 0.31$ and $b = 0.31$ from Masaki et al. (2006), a plot of the stress-strain curve in the apical-middle part of the tectorial membrane is shown (figure 7).

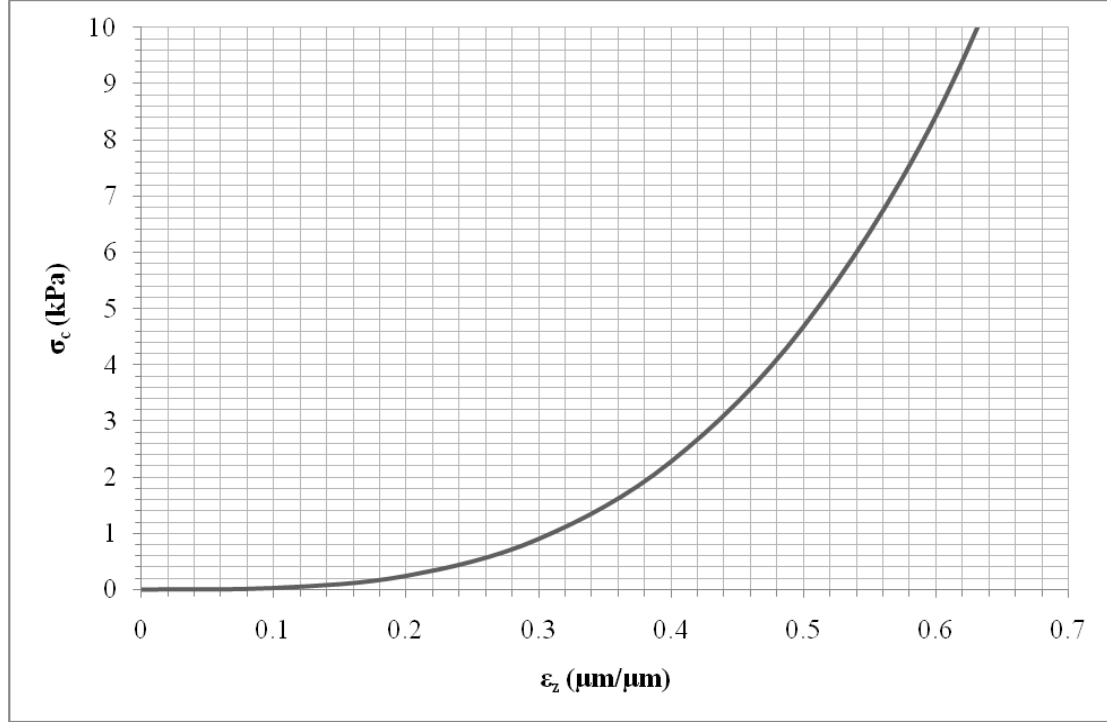


Figure 7. Plot of stress-strain curve of the apical-middle region of the tectorial membrane using constants $a = 0.31$ and $b = 0.31$ from Masaki et al. (2006).

Figure 7 clearly displays a stress-strain relationship that is almost completely non-linear and appears to resemble the stress-strain relationship of an elastomer (rubber) in tension. Figure 8 depicts the tensile stress-strain curves for four natural rubber compounds of different hardnesses as shown in Lindley (1966). The stress-strain curve of the tectorial membrane from figure 7 also seems to suggest nearly perfect elasticity, or that the strain is mostly recoverable. In addition to behaving like an elastomer, the tectorial membrane may also behave partially like a fluid.

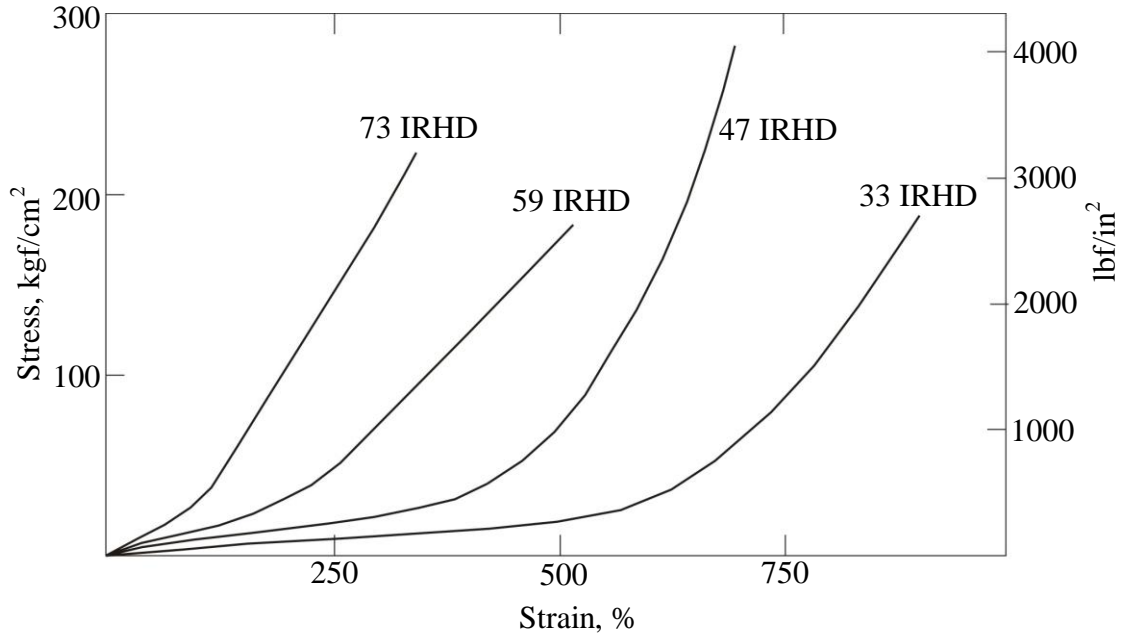


Figure 8. Tensile stress-strain curves for four natural rubber compounds of different hardnesses (adapted from Lindley 1966).

Since figure 7 is essentially non-linear, it appears as though it can be classified as a type V stress-strain curve as presented in Byars and Snyder (1969). For non-linear curves, the Ramberg-Osgood model can be used for determining the constitutive stress-strain relationship. This is presented below:

$$\varepsilon = \frac{\sigma}{E} + K \left(\frac{\sigma}{E} \right)^n \quad (9)$$

where, ε is the strain, σ is the stress, E is the Young's modulus and thus the slope of the tangent to the curve taken from the origin for a type V curve, and K and n are constants found from experimentation (Byars and Snyder 1969).

As mentioned previously in the chapter, different studies (Schoelson et al. 2004, Gueta et al. 2006; 2008, Richter et al. 2007, and Gavara and Chadwick 2009) have experimentally obtained Young's modulus. However, this section is concerned with

comparing the stress-strain relationship of an elastomer to that of the tectorial membrane. In the former, as the stress-strain relationship is non-linear, a distinct yield point is not well defined. Without an assumed yield point, Eq. (9) is not applicable. Additionally, Young's modulus for rubber is generally calculated for small strains. From figure 7, there is no obvious yield point for the tectorial membrane based on the power law in Eq. (8). Therefore, Eq. (9) does not apply here and Eq. (8) will be taken to be the constitutive stress-strain relationship of the tectorial membrane.

Damage of the Tectorial Membrane

When subjected to constant heavy sound stimulation (~120 dB), the tectorial membrane becomes damaged by being partially stretched. From Poje et al. (1995), the damage and repair of the tectorial membrane was thought to play a major role in hearing loss and recovery in chick ears when exposed to intense pure tones at 120 dBL. It is widely believed that due to acoustic trauma the extracellular matrix in the tectorial membrane breaks up (depolymerizes). This acoustic trauma produces a patch lesion, and at this spot the upper and lower layers of the tectorial membrane disintegrate until there is complete damage after 24 hours of exposure. The tectorial membrane also decouples from the hair cells during sound damage. Studies have shown that the tectorial membrane can repeatedly regenerate itself and form honeycomb patterns around each hair cell, but it never fully recovers its original structure (Adler et al. 1995; Contanche 1999; Ding-Pfennigdorf 1998; Kurian et al. 2003).

From Contanche 1992, tectorial membranes were taken from chicks and exposed to 1500 Hz pure tones at 120 dBL for a 24 hour period. Video-enhanced DIC images

were taken of the tectorial membrane immediately after exposure and also after a 14 day recovery period. Figure 9 depicts two video-enhanced DIC images. The image on the left, Fig. (9a), is the control tectorial membrane that is undamaged. As mentioned previously, the collagen fibrils in the tectorial membrane are oriented radially, and these can be seen in Fig. (9a). The image on the right, Fig. (9b) depicts the noise-damaged region of the tectorial membrane immediately after exposure. Here the tectorial membrane appears distorted and the lateral fibrils are wavy and not clearly defined. Specifically, the center of Fig. (9b) appears to be stretched as the distorted fibrils have shriveled away from it.

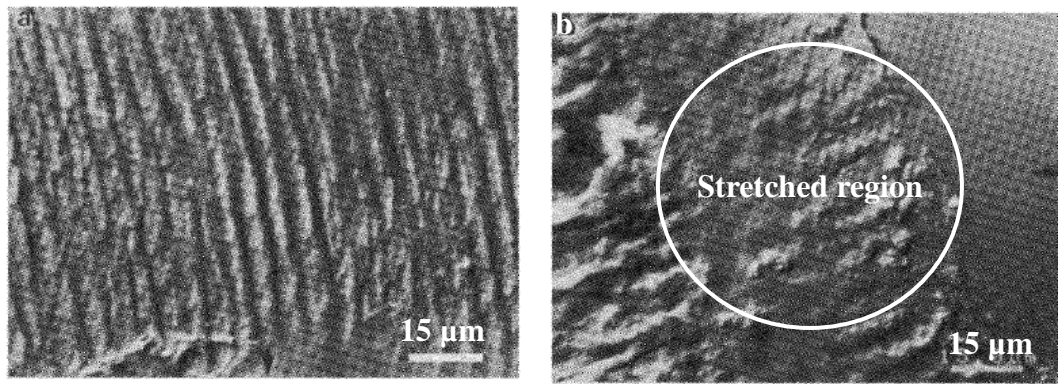


Figure 9. Video-enhanced DIC images of the tectorial membrane taken from Cotanche (1992): (a) control specimen; (b) specimen immediately after exposure to 1500 Hz pure tones at 120 dBL for a 24 hour period. The stretched region is marked in 7b.

The way in which the damaged portion of the tectorial membrane stretches in Fig. (9b) when subjected to heavy sound stimulation appears to be similar to the way that an elastomer stretches in tension. From Wang et al. (2002), uniaxial tension and fatigue tests were performed on rubber specimens. The fatigue tests were done under ambient conditions (22°C), and the samples were subjected to triangular cyclic strain waves with a frequency of 0.1 Hz. Figure 10 depicts SEM micrographs of the surface of two

different specimens. The image on the left, Fig. (10a) is the virgin (undamaged) sample, and the image on the right, Fig. (10b) is a sample subjected to 1600 cycles.

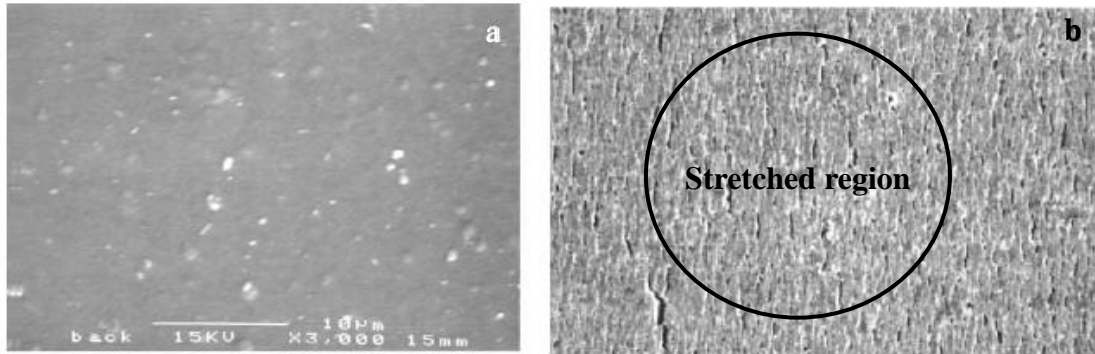


Figure 10. SEM micrographs of rubber of two different specimens taken from Wang et al. (2002): (a) virgin sample (x3000); (b) sample at 200% strain and subjected to 1600 cycles (x1000). Extensive microvoids can be seen in 8b.

Although the tectorial membrane and the elastomer samples clearly exhibit different physical behavior with the former depicting distorted fibrils and the latter depicting microvoids as evidenced in Fig. (9b) and Fig. (10b), respectively, they both apparently stretch when subjected to external forces. The distorted fibrils can also be considered as micro defects that may alter the tectorial membrane's stiffness.

The damage of the tectorial membrane can also be expressed graphically. Using Eq. (8) and data derived in figure 7, hysteresis loops are presented in figure 11 for the tectorial membrane when subjected to cycles of osmotic pressure. In figure 12, the hysteresis loops are presented for a purely viscoelastic computation of rubber damage when subjected to cyclic tension. As mentioned earlier in the chapter, studies have shown that the tectorial membrane displays viscoelastic properties. Thus, the hysteresis loops in both figures 11 and 12 further suggest that the tectorial membrane has similar mechanical properties to that of an elastomer.

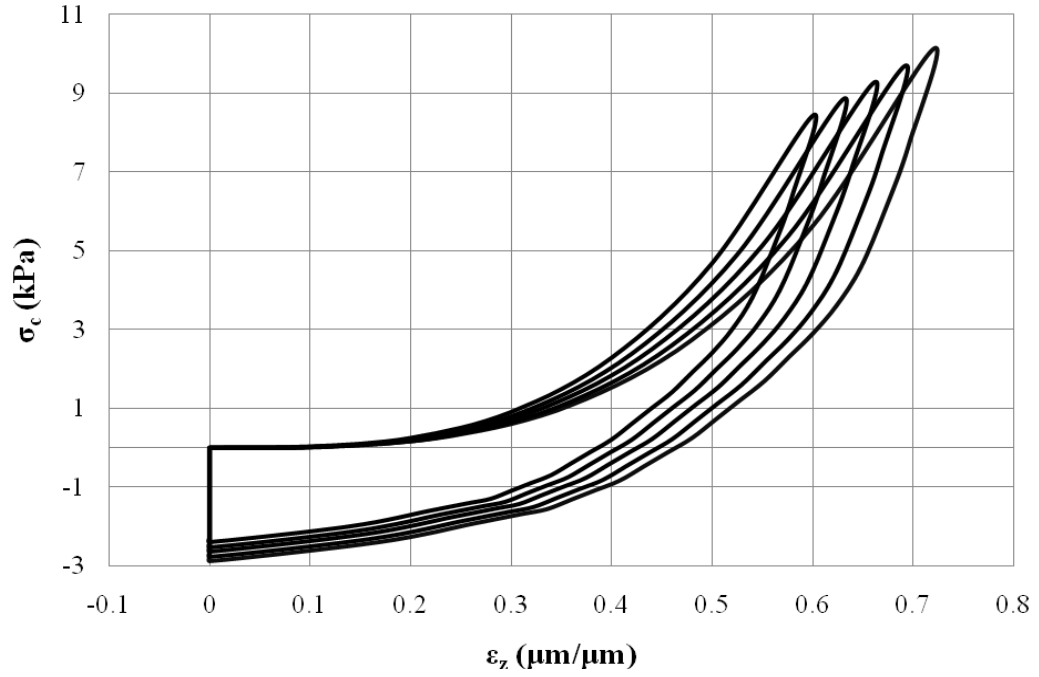


Figure 11. Hysteresis loops for the tectorial membrane when subjected to cycles of osmotic pressure.

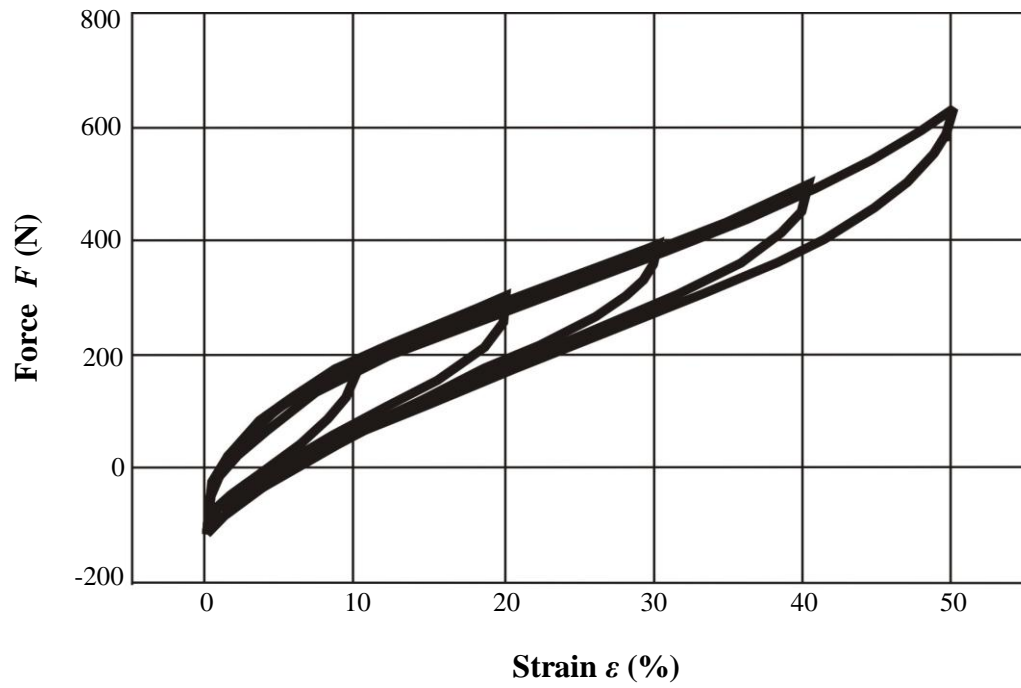


Figure 12. Hysteresis loops for a purely viscoelastic computation of rubber damage when subjected to cyclic tension.

As shown in figure 11, hysteresis loops graphically depict the potential quantitative damage of the tectorial membrane under cyclic loadings of osmotic pressure. The area contained within these loops is the quantitative damage as expressed in terms of strain energy density U_0 . Since it is difficult to determine a reliable yield point and subsequently a Young's modulus for the tectorial membrane, a Gibbs free energy approach can be used to quantify the damage from the hysteresis loops. The fundamental thermodynamic equation for Gibbs free energy is:

$$G(p,T) = H - TS = (U + pV) - TS \quad (10)$$

where, H is enthalpy, U is the internal energy in the system, p is pressure, V is volume, T is temperature, and S is entropy. The pressure p can be replaced with $\int \sigma d\varepsilon$ which is the term for strain energy density U_0 because stretching is assumed to be occurring in the tectorial membrane. Additionally, the variables T and S will be ignored because temperature and entropy, respectively, are assumed to not be relevant in this case. Therefore, the Gibbs free energy of the tectorial membrane $G(\varepsilon_z)$ can be rewritten as:

$$G(\varepsilon_z) = U(\varepsilon_z) = V_{TM} \oint \sigma_c d\varepsilon_z \quad (11)$$

where, $U(\varepsilon_z)$ is the internal strain energy, V_{TM} is the volume of the tectorial membrane, and therefore $\sigma_c d\varepsilon_z$ is the strain energy density integrated along the entire path of each hysteresis loop in figure 11. Table 1 presents the internal strain energy $U(\varepsilon_z)$ in μJ due to the number of cycles of applied osmotic pressure. This strain energy quantifies the amount of damage that the tectorial membrane undergoes with each subsequent cycle. The volume V_{TM} is assumed to be equivalent to $2.5 \times 10^6 \mu\text{m}^3$.

Table 1. Strain energy due to the number of cycles of applied osmotic pressure.

Number of cycles of osmotic pressure	$U(\varepsilon_z)$ (μJ)
1	2.83×10^{-3}
2	2.84×10^{-3}
3	3.58×10^{-3}
4	5.27×10^{-3}
5	7.99×10^{-3}

The stretching damage of the tectorial membrane has been established as equivalent to the internal strain energy of its hysteresis loop. Therefore, the applied external force such as a decibel pressure load from a wind farm on the tectorial membrane can then be determined by applying Castigliano's first theorem. The theorem states that for both linearly elastic and nonlinearly elastic structures the generalized force P_i can be calculated by:

$$P_i = \frac{\partial U}{\partial \delta_i} \quad (12)$$

where, ∂U and $\partial \delta_i$ are the partial derivatives of the strain energy and generalized displacement, respectively. Substituting Eq. (11) into Eq. (12), assuming an external force P_{ext} and displacement δ_z in the transverse z-axis, and balancing the energy terms by rearrangement results in the following equation of virtual work:

$$P_{ext} \delta_z = \sigma_{ext} A_{TM} \delta_z = U(\varepsilon_z) = V_{TM} \oint \sigma_c d\varepsilon_z \quad (13)$$

where, in addition to terms previously defined, σ_{ext} is the external decibel pressure and A_{TM} is the area of tectorial membrane in the x-y plane normal to the direction that the external decibel pressure is being applied. This area A_{TM} is assumed to be equivalent to $5 \times 10^4 \mu\text{m}^2$. Figures 13 presents the tectorial membrane modeled as a simply-supported

beam of length l , width w , and thickness t with an external force P_{ext} from a point source (i.e. wind farm) applied at midspan.

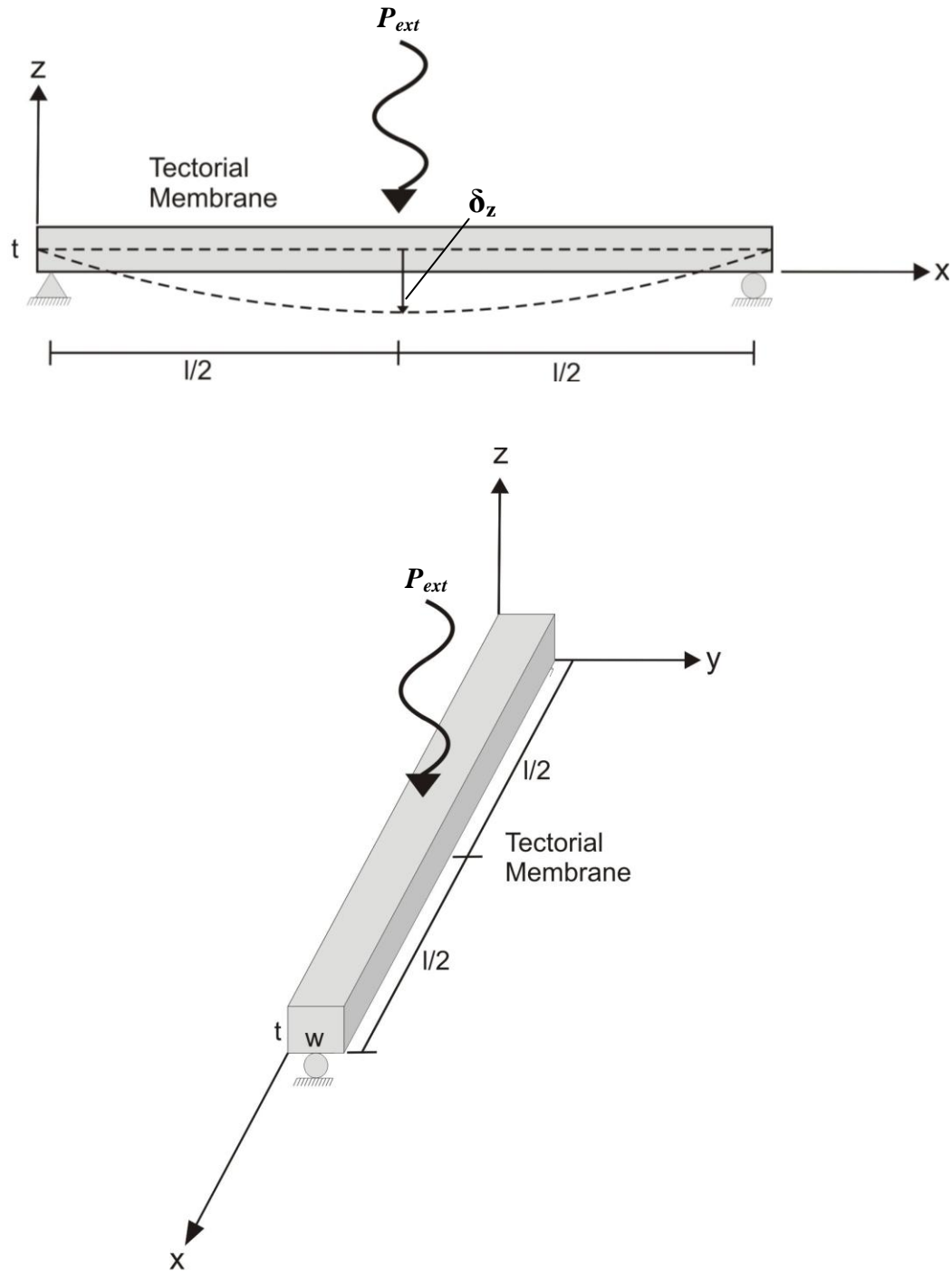
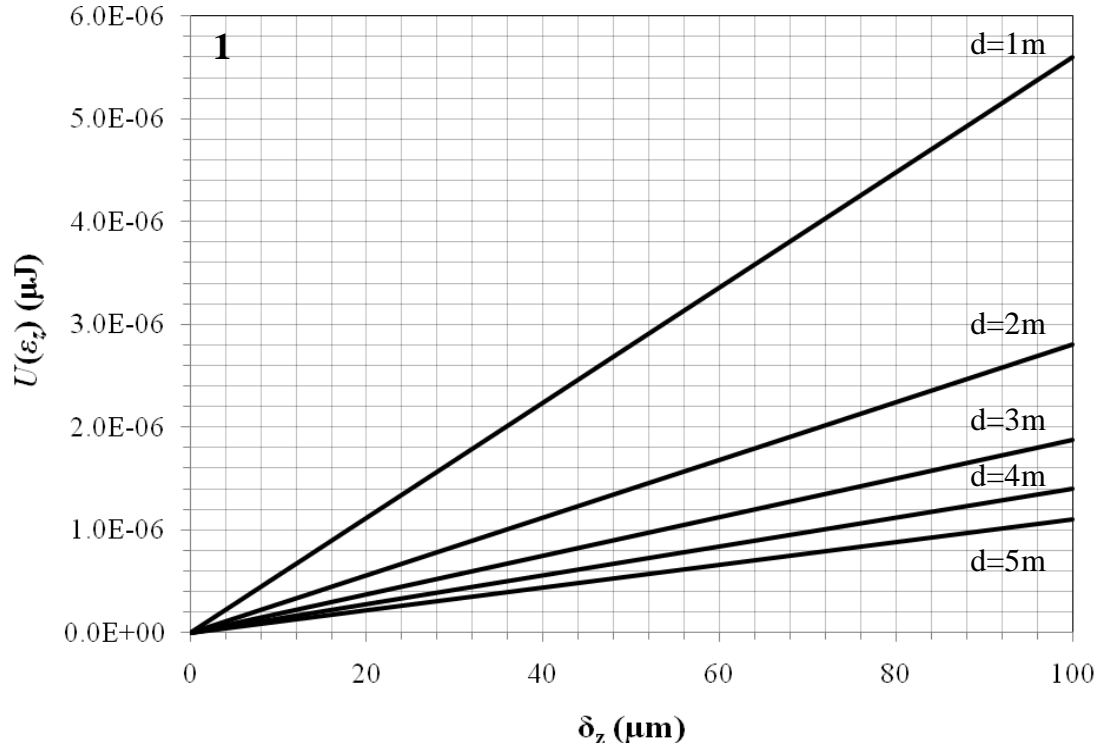


Figure 13. The tectorial membrane modeled as a simply-supported beam of length l , width w , and thickness t with an external force P_{ext} from a wind farm applied at midspan. The tectorial membrane displaces a distance δ_z under the loading at midspan.

From the energy balance in Eq. (13), the transverse z-axis displacement δ_z can be parametrically varied with an assumed constant decibel level and balanced with the internal strain energy of the tectorial membrane. This quantifies the amount of damage that the tectorial membrane undergoes with each increasing displacement. The external decibel pressure σ_{ext} is taken to be equivalent to each of the A-weighted dB values from the data in figure 5. The external force P_{ext} is equivalent to σ_{ext} multiplied by the area of the x-y plane of the tectorial membrane A_{TM} . Figure 14 presents multiple curves of the damage (internal strain energy) of the tectorial membrane that occurs with increasing transverse z-axis displacement δ_z . Each curve is for a different A-weighted external decibel pressure beginning with 95 dBA. This corresponds to a distance $d=1m$ away from the wind farm point source.



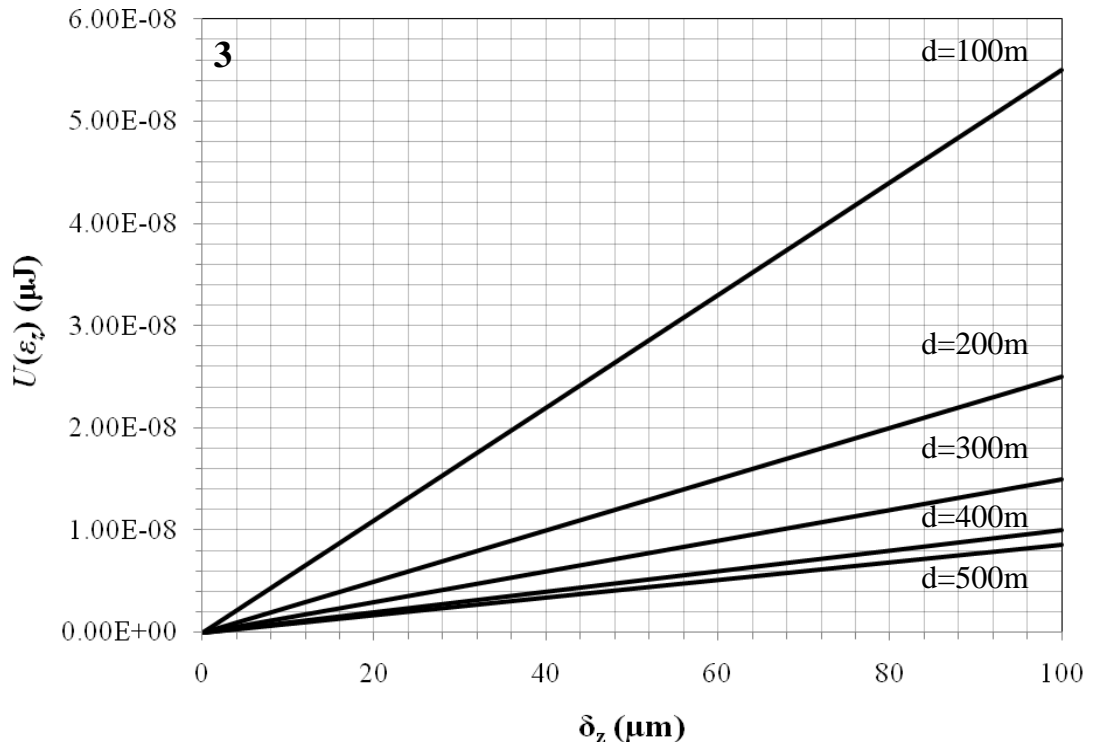
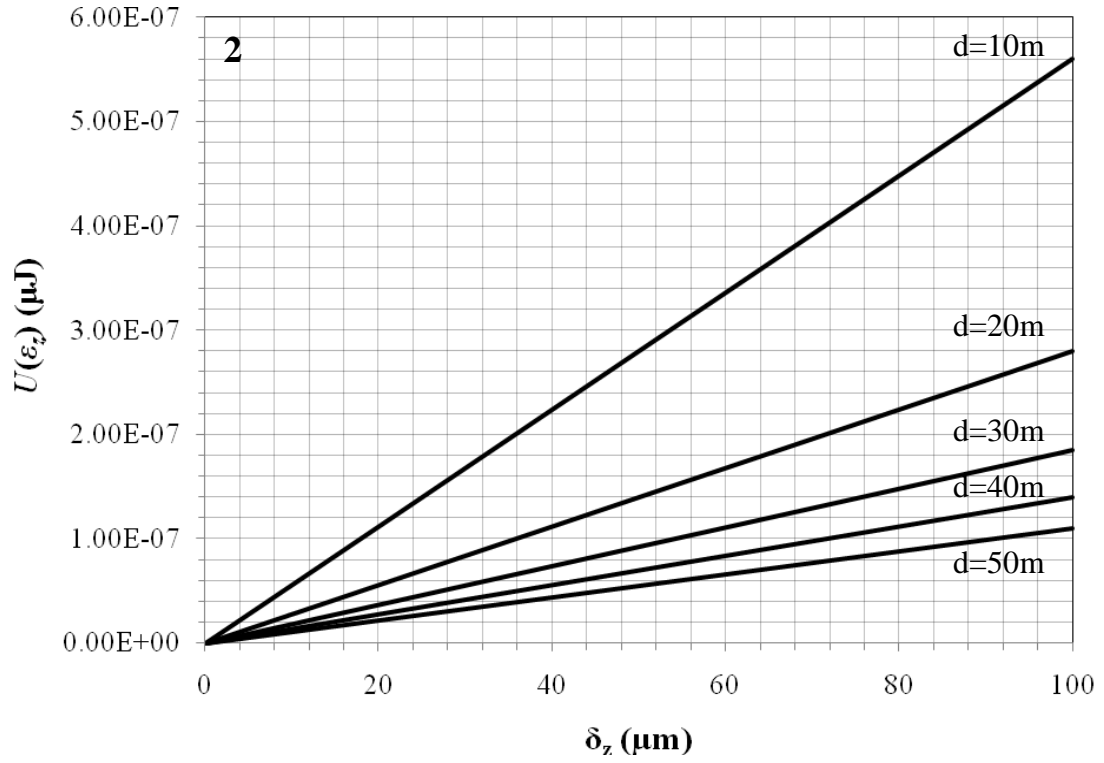


Figure 14. Damage of the tectorial membrane vs. the z-axis displacement.
 (1) $d = 1\text{-}5\text{m}$; (2) $d = 10\text{-}50\text{m}$; and (3) $d = 100\text{-}500\text{m}$ from a wind farm.

As mentioned previously and shown in figure 5, at a distance $d=500\text{m}$ away from the wind turbine point source, the perceivable A-weighted decibel value is 38 dBA. From Salt (2010), the wind turbine noise spectra curve shows an A-weighted decibel value of ~ 40 dBA at 700 Hz. Along the curve the unweighted wind turbine noise spectra data in the infrasound range (1-20 Hz) ranges between 90 and 60 dB, respectively. It is assumed that this noise spectra applies to a wind farm at a distance $d=500\text{m}$ away from the wind turbine point source. Thus, the damage of the tectorial membrane based on unweighted decibel values in the infrasound range with respect to the z-axis displacement at a distance $d=500\text{m}$ is presented in figure 15.

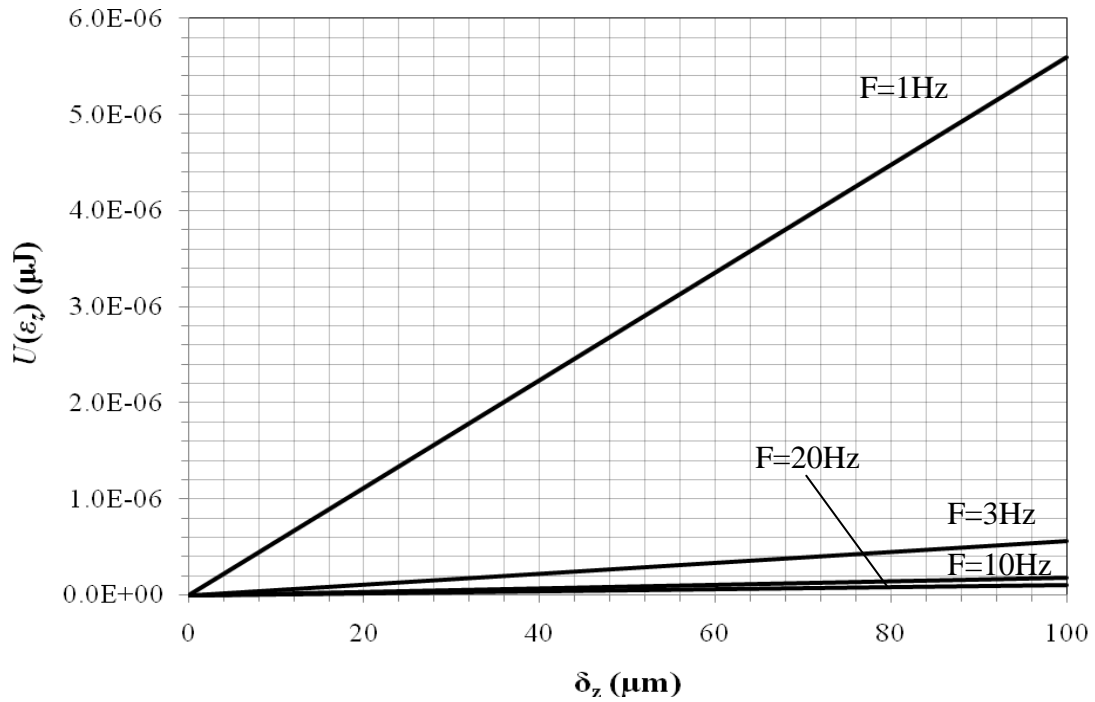


Figure 15. Damage of the tectorial membrane based on unweighted decibel values in the infrasound range vs. the z-axis displacement at a distance $d=500\text{m}$ from a wind farm. Frequencies range between 1 and 20 Hz.

Figure 14 quantifies the amount of damage in terms of strain energy that the tectorial membrane undergoes for increasing z-axis displacement at various distances away from a wind farm point source. These values can then be compared with $U_{\max}(\varepsilon_z)$, which is the maximum strain energy that the tectorial membrane can undergo before being overstretched and developing micro tears. Based on the rubber damage modeling equations in Kolling et al. (2005), the damage parameter D for the tectorial membrane is taken to be equivalent to:

$$D\left(\frac{U(\varepsilon_z)}{U_{\max}(\varepsilon_z)}\right) = 1 - \frac{\sigma_{ulcd}(\varepsilon_z)}{\sigma_{lcd}(\varepsilon_z)} \quad (14)$$

where, $\sigma_{ulcd}(\varepsilon_z)$ is the stress in the unloading curve, $\sigma_{lcd}(\varepsilon_z)$ is the stress in the loading curve, and the max internal strain energy is:

$$U_{\max}(\varepsilon_z) = V_{TM} \int_0^{\varepsilon_{z,\max}} \sigma_{lcd} d\varepsilon_z \quad (15)$$

The area under the loading part of the hysteresis loop in figure 11 multiplied by the volume of the tectorial membrane V_{TM} is equivalent to $U_{\max}(\varepsilon_z)$. However, it is not known whether or not an applied stress of 10 kPa as done by Masaki et al. (2006) exceeds the allowable maximum strain energy of the tectorial membrane. Therefore, using 120 dB (20 Pa) as the maximum allowable stress on the tectorial membrane based on the stretching damage shown in figure 9, $U_{\max}(\varepsilon_z)$ is 5×10^{-5} μ J. Based on Eqn. (14) and the data from figure 14, table 2 presents the damage parameter D of the tectorial membrane vs. the distance d away from a wind farm point source for transverse z-axis displacements δ_z between 10 and 100 μ m. Figure 16 presents the results from the table graphically.

Table 2. Damage parameter D of the tectorial membrane vs. distance d away from a wind farm point source for transverse z -axis displacements δ_z between 10 and 100 μm .

$\delta_z = 10\mu\text{m}$		$\delta_z = 20\mu\text{m}$		$\delta_z = 30\mu\text{m}$		$\delta_z = 40\mu\text{m}$		$\delta_z = 50\mu\text{m}$	
d (m)	D	d (m)	D	d (m)	D	d (m)	D	d (m)	D
1	1.1E-02	1	2.2E-02	1	3.4E-02	1	4.5E-02	1	5.6E-02
10	1.1E-03	10	2.2E-03	10	3.4E-03	10	4.5E-03	10	5.6E-03
20	5.6E-04	20	1.1E-03	20	1.7E-03	20	2.2E-03	20	2.8E-03
30	3.7E-04	30	7.4E-04	30	1.1E-03	30	1.5E-03	30	1.9E-03
40	2.8E-04	40	5.6E-04	40	8.4E-04	40	1.1E-03	40	1.4E-03
50	2.2E-04	50	4.4E-04	50	6.6E-04	50	8.8E-04	50	1.1E-03
60	1.8E-04	60	3.6E-04	60	5.5E-04	60	7.3E-04	60	9.1E-04
70	1.6E-04	70	3.1E-04	70	4.7E-04	70	6.2E-04	70	7.8E-04
80	1.4E-04	80	2.7E-04	80	4.1E-04	80	5.4E-04	80	6.8E-04
90	1.2E-04	90	2.4E-04	90	3.6E-04	90	4.8E-04	90	6.0E-04
100	1.1E-04	100	2.2E-04	100	3.3E-04	100	4.4E-04	100	5.5E-04
200	5.0E-05	200	1.0E-04	200	1.5E-04	200	2.0E-04	200	2.5E-04
300	3.0E-05	300	6.0E-05	300	9.0E-05	300	1.2E-04	300	1.5E-04
400	2.0E-05	400	4.0E-05	400	6.0E-05	400	8.0E-05	400	1.0E-04
500	1.7E-05	500	3.4E-05	500	5.1E-05	500	6.8E-05	500	8.5E-05

$\delta_z = 60\mu\text{m}$		$\delta_z = 70\mu\text{m}$		$\delta_z = 80\mu\text{m}$		$\delta_z = 90\mu\text{m}$		$\delta_z = 100\mu\text{m}$	
d (m)	D	d (m)	D	d (m)	D	d (m)	D	d (m)	D
1	6.7E-02	1	7.8E-02	1	9.0E-02	1	1.0E-01	1	1.1E-01
10	6.7E-03	10	7.8E-03	10	9.0E-03	10	1.0E-02	10	1.1E-02
20	3.4E-03	20	3.9E-03	20	4.5E-03	20	5.0E-03	20	5.6E-03
30	2.2E-03	30	2.6E-03	30	3.0E-03	30	3.3E-03	30	3.7E-03
40	1.7E-03	40	2.0E-03	40	2.2E-03	40	2.5E-03	40	2.8E-03
50	1.3E-03	50	1.5E-03	50	1.8E-03	50	2.0E-03	50	2.2E-03
60	1.1E-03	60	1.3E-03	60	1.5E-03	60	1.6E-03	60	1.8E-03
70	9.3E-04	70	1.1E-03	70	1.2E-03	70	1.4E-03	70	1.6E-03
80	8.1E-04	80	9.5E-04	80	1.1E-03	80	1.2E-03	80	1.4E-03
90	7.1E-04	90	8.3E-04	90	9.5E-04	90	1.1E-03	90	1.2E-03
100	6.6E-04	100	7.7E-04	100	8.8E-04	100	9.9E-04	100	1.1E-03
200	3.0E-04	200	3.5E-04	200	4.0E-04	200	4.5E-04	200	5.0E-04
300	1.8E-04	300	2.1E-04	300	2.4E-04	300	2.7E-04	300	3.0E-04
400	1.2E-04	400	1.4E-04	400	1.6E-04	400	1.8E-04	400	2.0E-04
500	1.0E-04	500	1.2E-04	500	1.4E-04	500	1.5E-04	500	1.7E-04

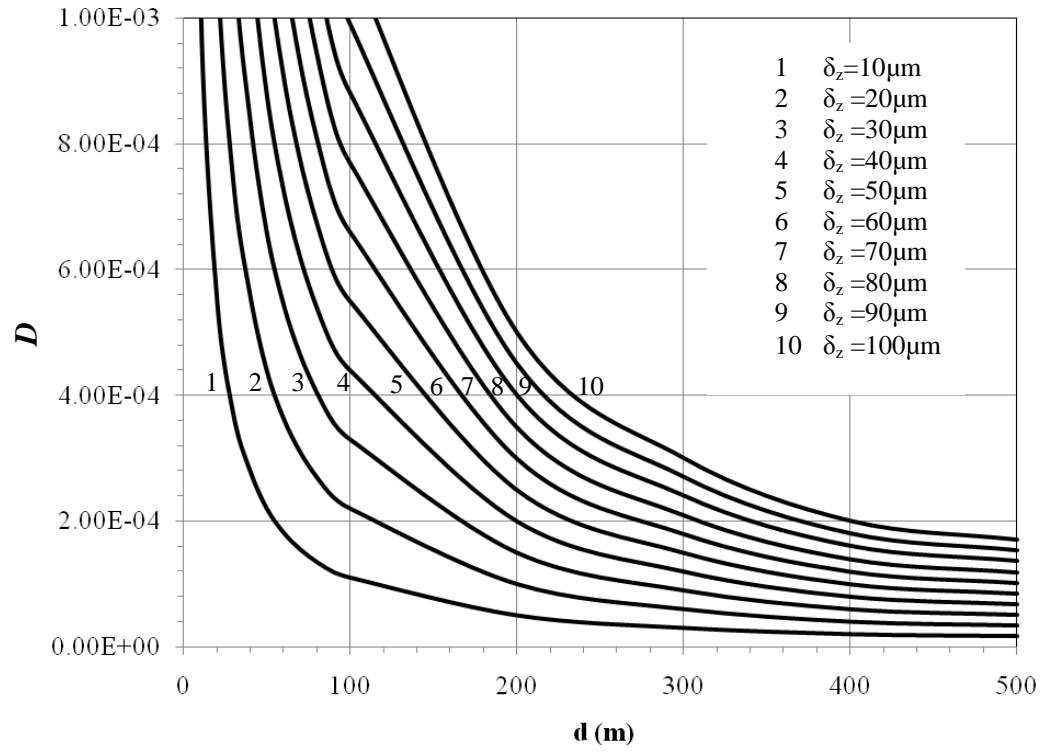


Figure 16. Damage parameter D of the tectorial membrane vs. distance d (m) for displacements δ_z between 10 and 100 μm .

CHAPTER 3

NEXT-GENERATION AUTONOMOUS HOUSING

Chapter Overview

In the modern building construction age, it has become attractive to supplement diminishing fossil fuel resources with intelligent housing systems that can have renewable energy capabilities. The challenge is to create sustainable building designs that are not only of higher quality but provide higher standards of living with minimal environmental impact. Thus, this chapter considers the novel concept of next-generation autonomous housing. In order to understand autonomous housing as a concept, it is important to first consider it as an individual self-sufficient unit or house. Then this idea can be expanded to understand it in the context of an entire self-sustaining village. In this chapter, a hypothetical autonomous village is considered. It contains about 2000 people (~500 families) and consists of round “beehive” housing communes with L-shaped modules that plug in to the overall structure. Nearby, there is a 2.5 MW wind farm that partially powers the village by providing it with electricity for hot water. An extensive architectural and design process was used in designing and planning the village, and this is described in detail. In the end of this chapter, the results from the damage modeling section of Chapter 2 are applied to suggest minimum safe distances between the wind farm and the village in the context of limiting damage to the tectorial membrane.

The Autonomous House

The autonomous building concept, which was first proposed in 1972 by Alexander Pike at the University of Cambridge School of Architecture, refers to a [building] not linked to the mains services of gas, water, electricity or drainage, but instead uses the income-energy sources of sun, wind, and rain to service itself and process its own wastes (Vale and Vale 2000). Autonomous buildings reduce ownership costs, carbon footprints, and overall environmental impact by eliminating dependence on public utilities and services. Current examples of autonomous housing include the Hockerton Housing Project, the Findhorn Eco-Village, and Earthships (Figure 17).



Figure 17. Current examples of autonomous housing. (1) Hockerton Housing Project in Hockerton, Nottinghamshire, UK; (2) Findhorn Eco-Village house in Moray, Scotland; (3) Earthship in Rio Arriba County, New Mexico.

Cost-Modeling the Autonomous House

Autonomous projects generally have the following characteristic features: (1) clean energy generation, storage, and use, (2) water collection and reuse, (3) sustainable food production, (4) the use of “green” construction materials, (5) the use of innovative building structures, and (6) resource availability. A technical cost-model can be used to simulate single autonomous buildings or houses. This model can generate fixed and variable costs for the six characteristic variables mentioned above. Figure 18 depicts an example of process-based cost model methodology for an autonomous house.

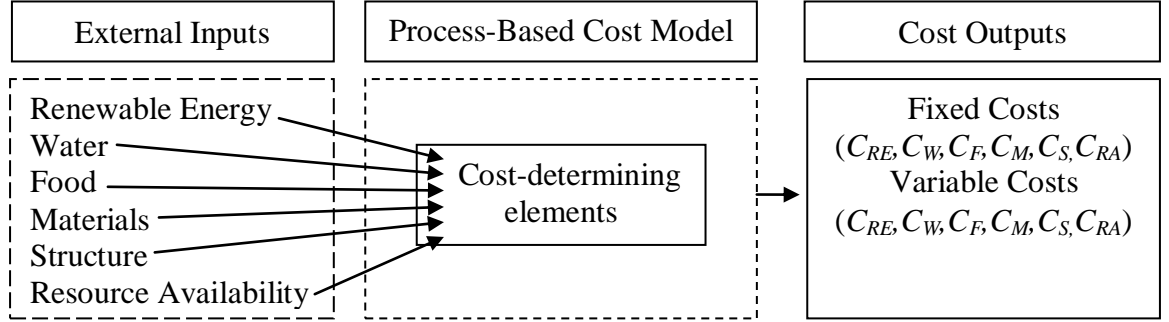


Figure 18. Example of process-based cost model methodology.

Based on the previous methodology, a general process-based cost model (PBCM) can be expressed as:

$$C_T = \sum_{i=1}^6 C_i, i = RE, W, F, M, S, RA \quad (16)$$

where C_T is the total cost over a certain time, C_{RE} is the cost of renewable energy resources, C_W is cost of water resources, C_F is the cost of food production, C_M is the cost of materials (e.g. Cenocell™ based materials, other concrete substitutes, etc.), C_S is the cost of structures, and C_{RA} is the cost of resource availability. Due to uncertainty and variation in the cost-modeling process, non-equilibrium and extreme-value statistical

methods will be used for estimating the total costs. An extreme-value equation for expected total cost, $E[C]$, is proposed here:

$$E[C] = \sum_{i=1}^6 n \times C_i = \left(n \int_{-\infty}^{+\infty} x \cdot [F(x)]^{n-1} \cdot f(x) dx - c \cdot n \right) \quad (17)$$

where n is the six input variables multiplied by the cost C_i of each one modeled using the cumulative distribution function from Dahan and Mendelson (2001). Assuming this model is reliable, different variable combinations can be simulated to create optimized, cost-efficient solutions that vary based on controlled parameter changes.

Principles of Cube Symmetry and Modular Design

As the idea of the autonomous house has been established previously, the design and layout of the autonomous village consisting of beehive housing communes will be discussed in the following sections. In designing these communes for the village, principles of cube symmetry and modular design were primarily employed. The former of these principles refers to the multiple forms of symmetry that exist in one of the simplest spatial shapes, the cube. The work of Stiny (1980), which is known as the “kindergarten grammars”, derives a series of geometrical *gifts* from Frederick Froebel’s *kindergarten method*. In four of the gifts (3-6), six individual solids are derived with the first one being the cube (Economou 1999). Furthermore, the structure of the cube contains multiple isometries that can be explored. From Economou and Baker (2006), there are ninety-eight symmetry groups of the structure of the cube. Additionally, the structure of the cube consists of the octahedral group which contains thirty-three conjugacy classes. The ninety-eight subgroups are formed from these conjugacy classes. Three of the ninety-eight configurations (classes) are depicted in Figure 19.

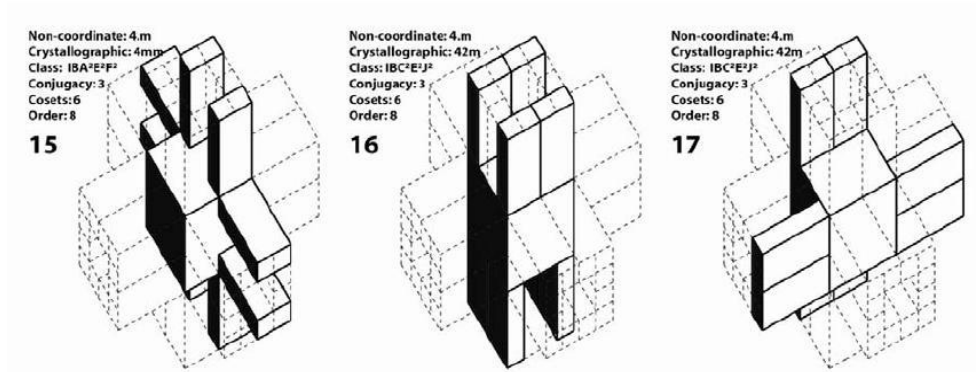


Figure 19. Three classes of the ninety-eight cube configurations (Economou and Baker 2006).

Modular design and construction feature individual pre-fabricated units that are combined together and installed on site to create an entire building structure. Advantages of modular construction include: (1) lower costs due to repeated manufacture of units, (2) increased installation speed, (3) more precise manufacturing, and (4) the ability to dismantle and reuse the constructed units. These units are usually considered as load-bearing elements where the loads are transferred through the walls. Modular construction is used in mid-rise cellular buildings (up to eight stories) that feature load-bearing walls that resist wind-induced shear forces. In high-rise buildings, modules that resist compression can be “clustered” around a core structure, which consequentially stabilizes them (Lawson and Richards 2010).

Prominent examples of modular design in architecture include Moshe Safdie’s Habitat ’67 (Figure 20) and Kisho Kurokawa’s Nakagin Capsule Tower (Figure 21). Both of these projects feature the cube as an individual unit. In his Habitat ’67, Safdie

combines pre-fabricated cubes to form an L-shaped motif and creates offset stacking configurations. Habitat '67 was designed as part of the 1967 International and Universal Exposition in Montreal, Canada. In his Nakagin Tower, which is one of the most prominent forms of Japanese “Metabolism” architecture, Kuroka employs the individual cube and stacks it repeatedly in organic forms to give the impression of a “growing” structure. In essence these cubes are “plugged” into an overall high-rise core structure in the method similar to that described by Lawson and Richards (2010).

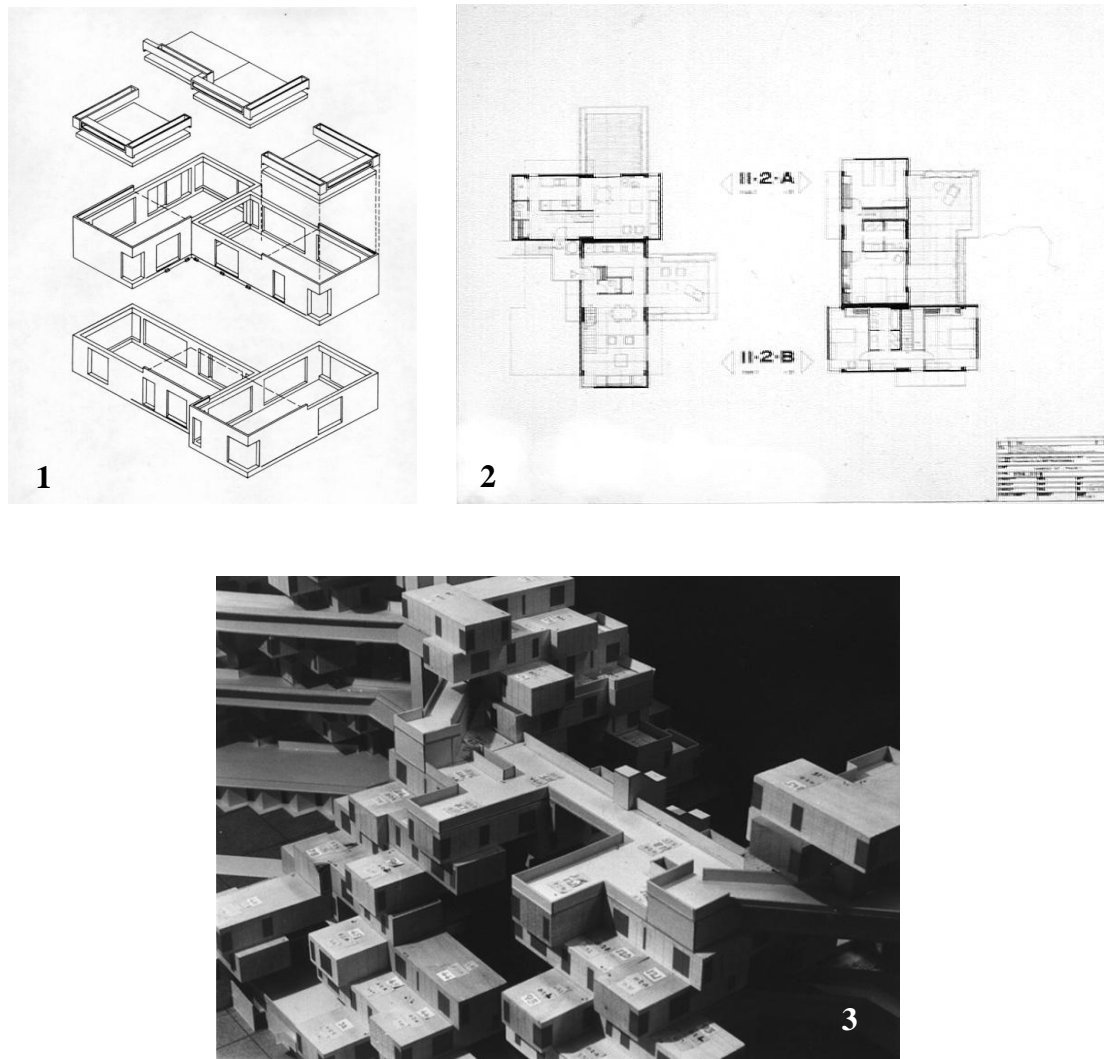


Figure 20. Exploded axonometric (1), plans (2), and stacking model (3) of the module cubes in Habitat '67 (Canadian Architecture Collection, McGill University 2001).

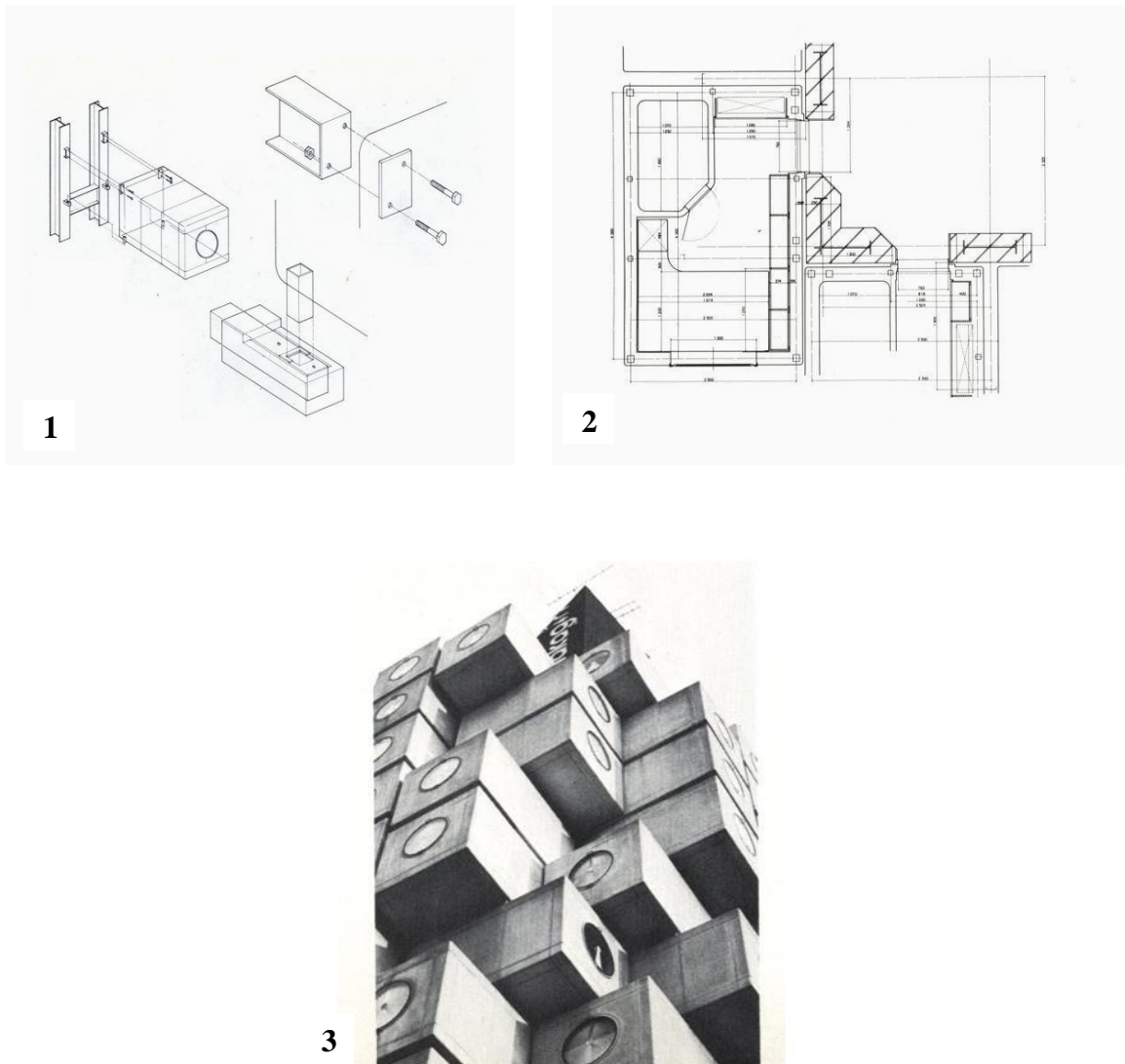


Figure 21. Axonometric (1), plan (2), and stacking arrangement (3) of the prefab modular capsule in Nakagin Tower (Kurokawa 1977; Schmal et al. 2005; Ross 1978).

Design of the L-module – Use of the Cube

In designing the L-module for the beehive structures, the structure of the cube was utilized extensively. A majority of the design for the modules was inspired from the two precedent projects mentioned previously (Habitat '67 and the Nakagin Tower). Each L-module is approximately 972 square feet and can house a family of 4-5 people.

Additionally, each one features 2 bedrooms, 2 bathrooms, a living room, a kitchenette, and a balcony. Figure 22 depicts a 3D model of the L-module.

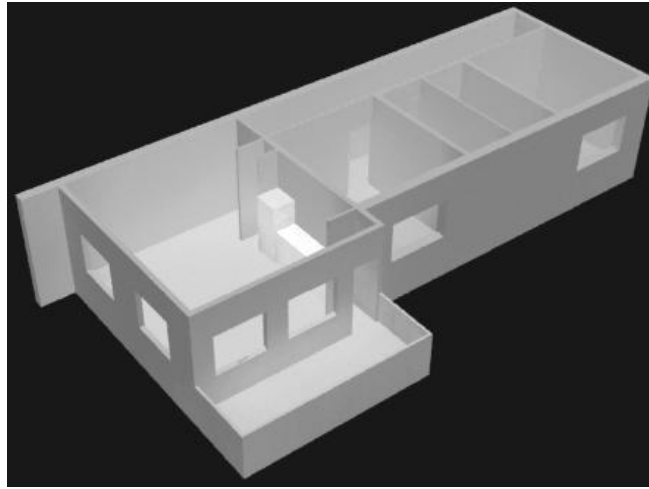


Figure 22. 3D model of the L-module (generated in Autodesk 3ds Max).

Figure 23 depicts the plan and section cuts of the L-module.

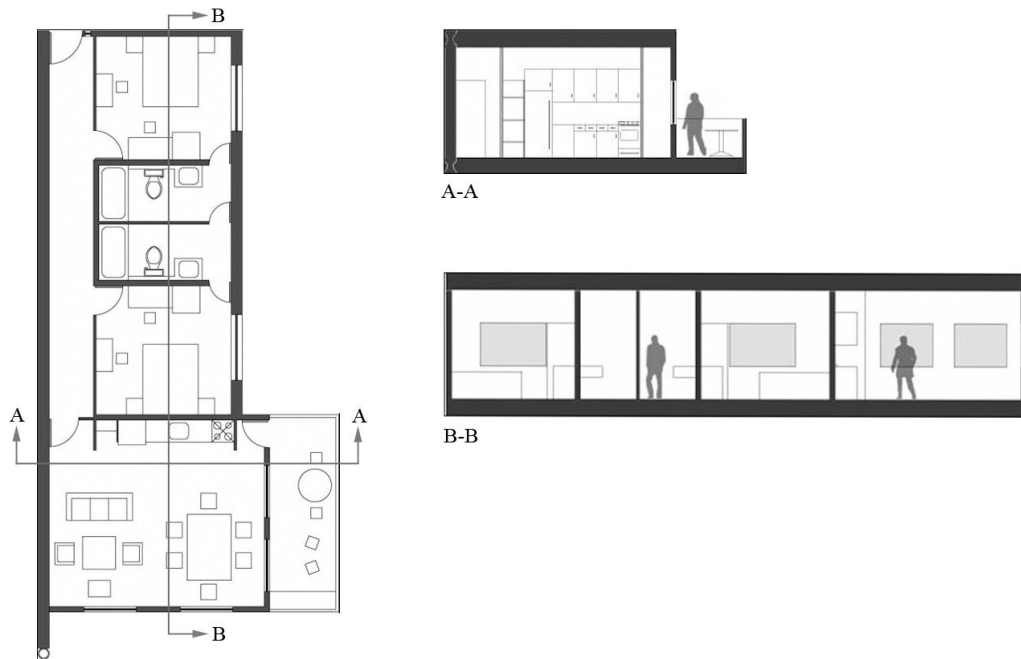


Figure 23. Plan and section cuts of the L-module.

The L-modules were then arranged to give the impression that they are “stacked.” In reality these modules are slid in between two core structural walls and “locked” in place. Shear releases are placed at each floor level to allow for sway due to lateral forces. For greater rigidity, these shear releases can be bolted in place. Figure 24 depicts the modules being stacked, while figure 25 illustrates how the modules are locked into place.

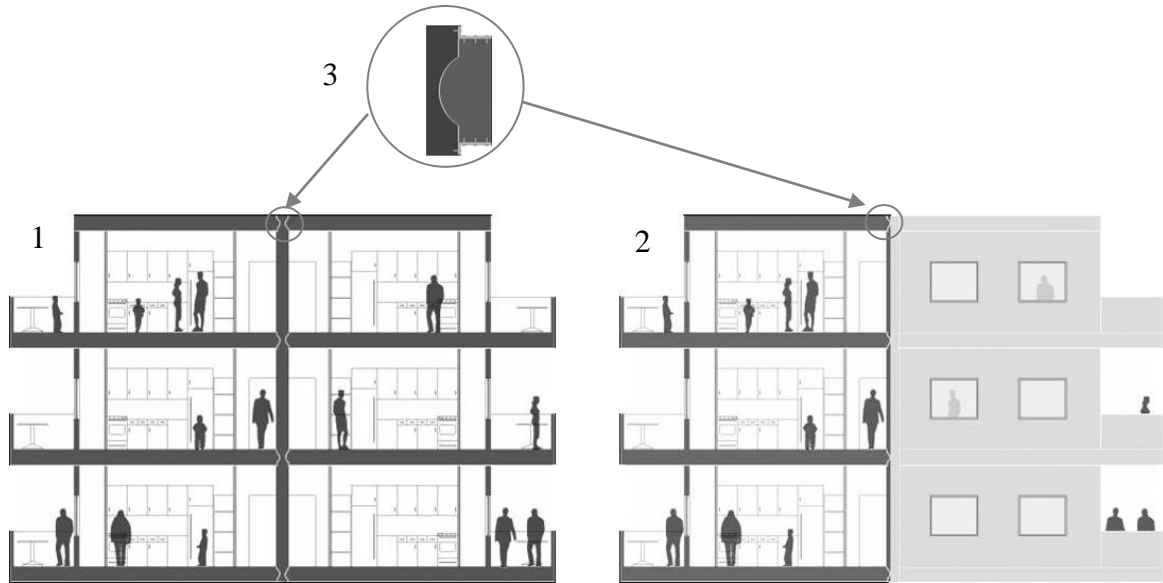


Figure 24. (1) Section cut of modules being stacked with (2) elevation of façade; (3) detail of shear release.

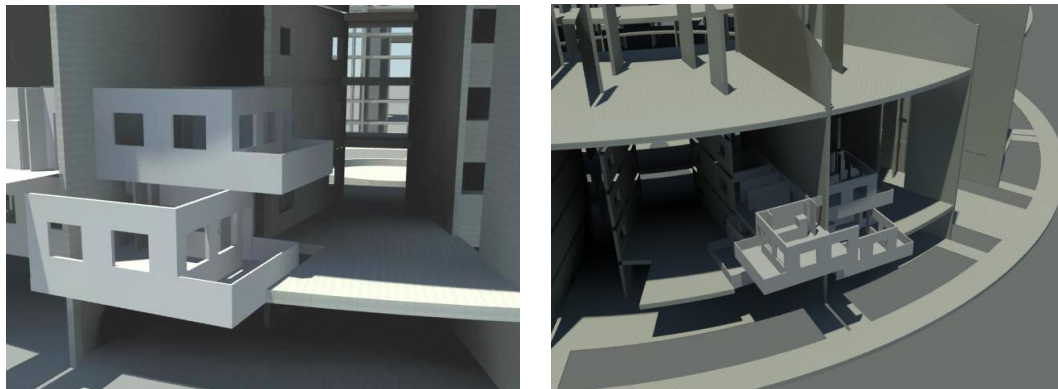


Figure 25. Modules being locked into “core” structure (generated in Autocad 3ds Max).

Design of the “Beehive” Structure – Zulu Design, Shells, and Rotational Symmetry

In designing the “beehive” structures, designs of traditional Zulu “beehive” dwellings were utilized. Some examples of these Zulu beehive dwellings are shown in figure 26.



Figure 26. Examples of Zulu beehive dwellings. (1) Traditional Zulu house, South Africa; (2) Two of the round houses on the Palace Grounds of the Zulu King; (3) Zulu “beehive” houses, Zululand, South Africa; (4) Traditional Zulu house, central Drakensberg, South Africa.

A defining principle behind the design of “beehive” commune is the use of rotational symmetry. As a precedent, Pier Luigi Nervi’s Palazzetto dello sport was studied for its use of rotational symmetry as well as for its use of a prefabricated reinforced ribbed concrete shell for the dome (figure 27).



Figure 27. (1) Ribbed reinforced concrete shell and (2) shell braced by concrete “Y” flying buttresses in the Palazzetto dello sport.

From Steadman and March (1971), there are three classes of plane symmetry groups based on their translational structure: (1) two planar *point groups*, (2) seven *frieze groups*, and (3) seventeen *wallpaper groups*. The two planar point groups, which have finite symmetry groups of rotation in the plane, are the *cyclic group* and the *dihedral group*. They do not contain any translations and can be represented by:

$$C_1, C_2, C_3, \dots, C_n, \dots \quad (18)$$

$$D_1, D_2, D_3, \dots, D_n, \dots$$

where, n is the period of the group, specifically the number of $360^\circ/n$ rotations for completing a full revolution. This was an important system set up by Leonardo da Vinci when he studied the symmetry of the core of a central building (Steadman and March 1971). The two planar point groups are depicted in figure 28; the cyclic group (left) contains rotations about the origin point up to $2\pi/n$, and the dihedral group (right) contains rotations and reflections about the origin point. The highlighted dihedral column served as a precedent for the “beehive” commune layout, particularly D_6 .

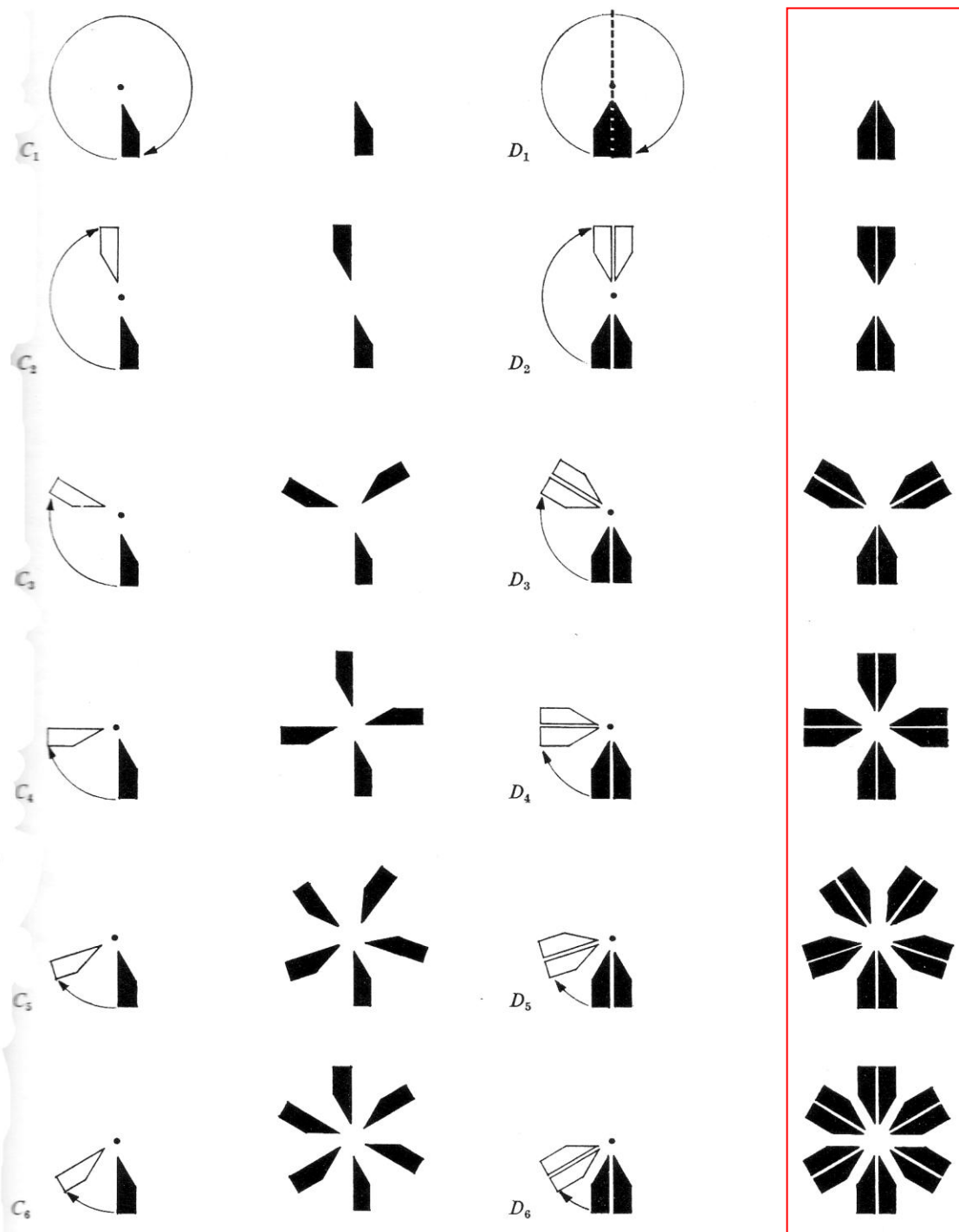


Figure 28. The two planar point groups: cyclic (C_n) and dihedral (D_n) (Steadman and March 1971).

Figure 29 depicts examples of point groups in architectural plans. Examples a-e are designs of Claude-Nicolas Ledoux and reflect the dihedral group: D_1 , D_2 , D_3 , D_4 , and D_{12} , respectively. Design e (D_{12}) is highlighted because it served as a direct precedent in the design of the beehive commune.

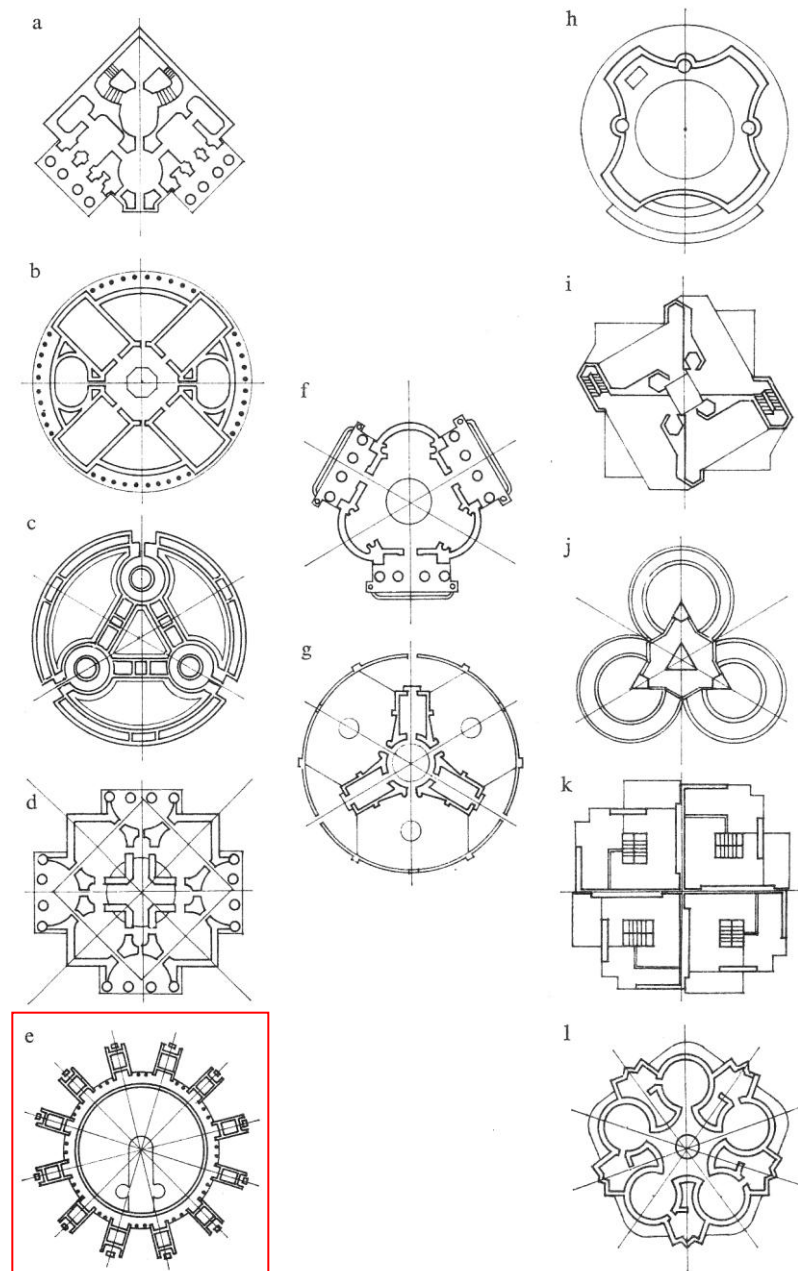


Figure 29. Examples of point groups in architectural plans (Steadman and March 1971).

A typical floor plan of the beehive commune is shown in figure 30. The design maintains the dihedral grouping (D_{14}) of symmetric rotation.

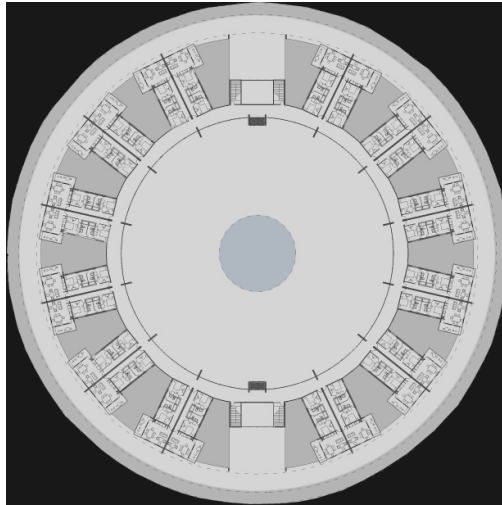


Figure 30. A typical floor plan of the beehive commune.

Figures 31 and 32 depict the overall structural model (with a spanning shell) and the module arrangement of the beehive commune, respectively.

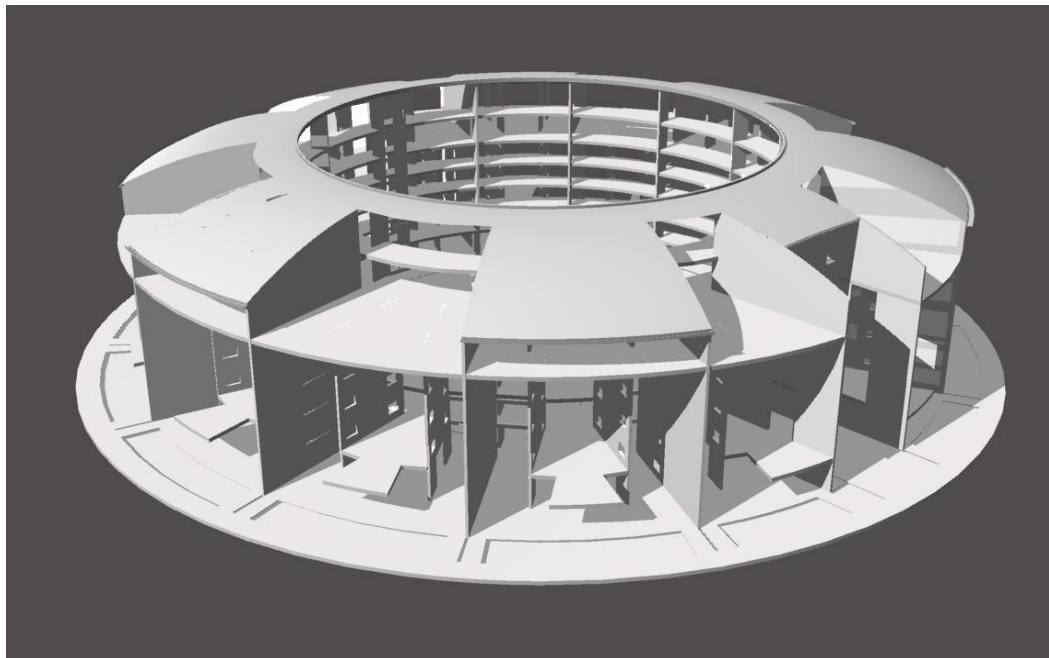


Figure 31. Complete structural model (generated in Rhinoceros 3D).



Figure 32. Module arrangement within the building (generated in Rhinoceros 3D).

A complete model of the beehive commune is generated in figure 33.

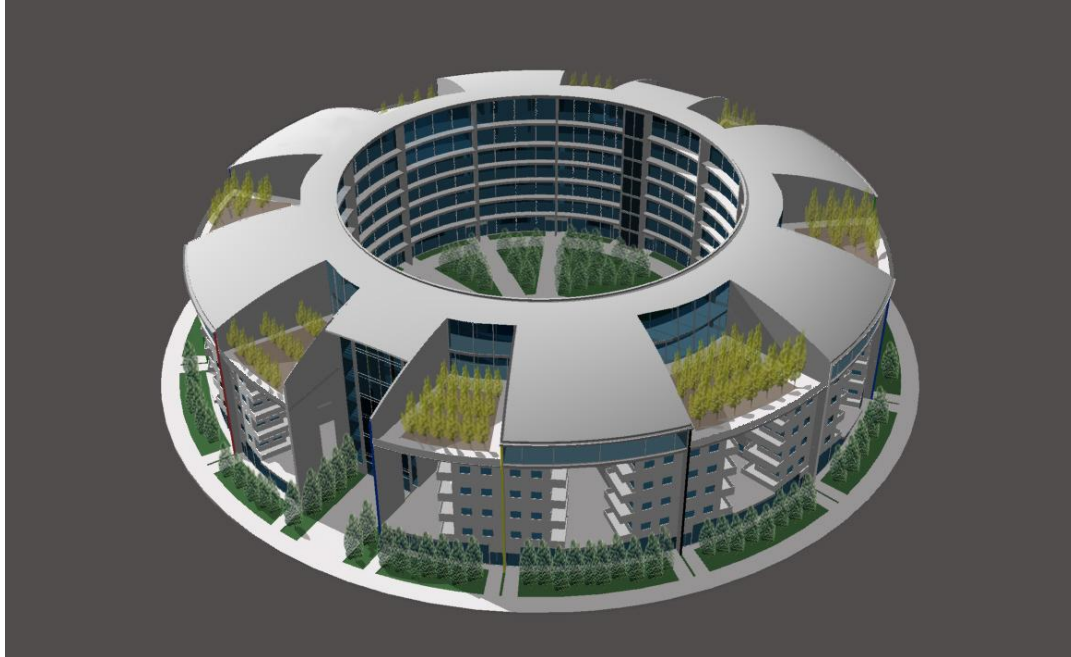


Figure 33. Complete view of the beehive commune (generated in Rhinoceros 3D).

Design of the Village – Zulu Layout and Group Symmetry

The first concept used in designing the village was utilizing the layout of historic Zulu settlements. An example of the layout of a Zulu royal settlement, Mgungundlovu is seen in figure 34. As is seen in the figure, the region bounded by E (known as Indlunkulu) housed the royalty including the king and his family. The ring-shaped regions marked 'N' and bounded by 'W' on either side of the settlement housed the soldiers. Cattle were kept within the open space in the center of the village and milked at the three enclosures marked 'R' (Kuper 1993).

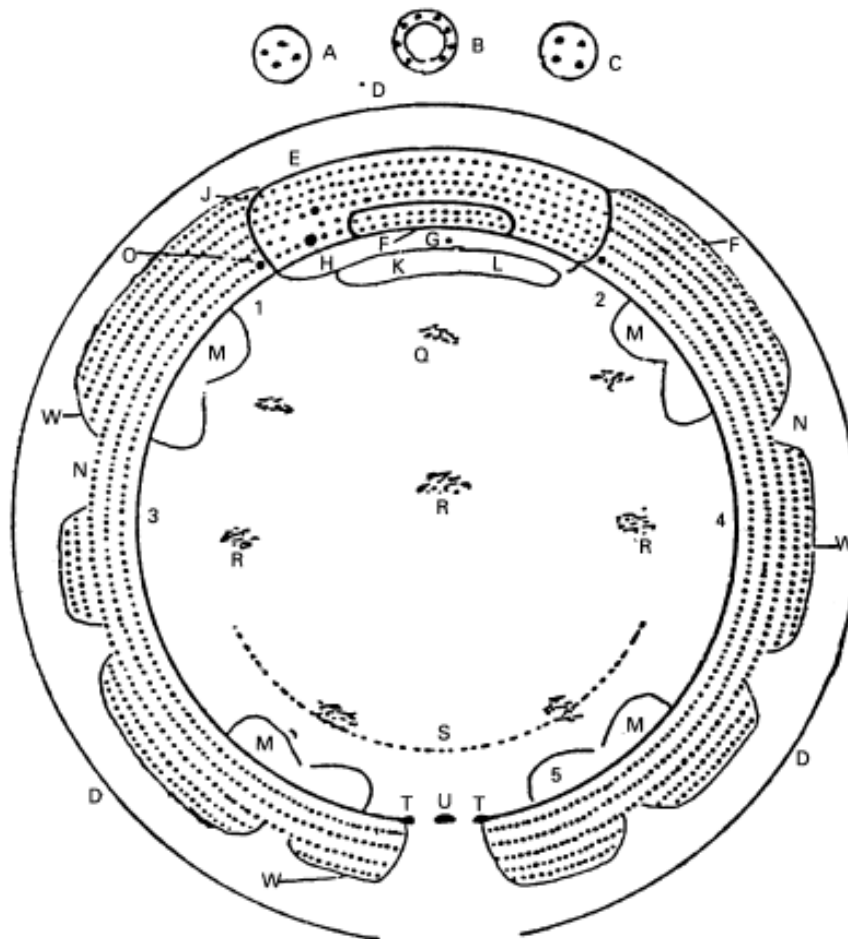


Figure 34. Layout of the Zulu royal settlement - Mgungundlovu (Kuper 1993).

Figure 35 depicts a layout of a traditional Zulu homestead. The hut marked 1 is the *Indlunkulu*, which was the largest of the huts and was associated with the head of the homestead. The head of the homestead actually lived in the house marked 2 (*Ilawu*), but his mother or great wife lived in the *Indlunkulu*. The *Indlunkulu* was the keystone and unified the homestead. Additionally, it housed ritual objects and served as a building to connect with the ancestors. As in the previous layout, the center of the homestead was where the cattle were kept as labeled in the figure as *cattle-byre* (Kuper 1993).

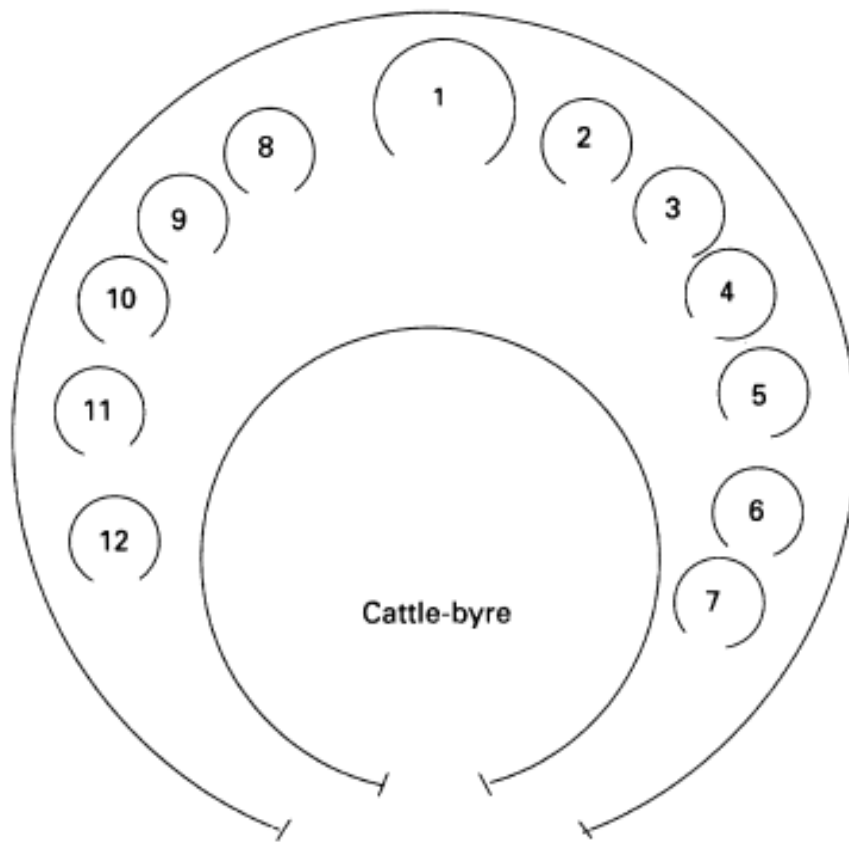


Figure 35. Layout of a Zulu homestead (Kuper 1993).

In addition to the influence of historic Zulu settlement layouts, the group symmetry concepts discussed by Steadman and March (1971) were also applied. The seventeen wallpaper groups are the third class of the plane symmetry groups and consist of more than one translation. There are two distinct translations (T_1 and T_2) that can be derived from any translation combination within a plane. In crystallographic restriction, the only possible periods of rotational symmetry are 2, 3, 4, and 6. The translations, T_1^i and T_2^j form a lattice that serves as the basis from any planar symmetric group, where i and j are integers ($i, j \in \mathbb{Z}$) (Steadman and March 1971). Figure 36 depicts W_6^1 , which refers to six point rotations and one direct translation.

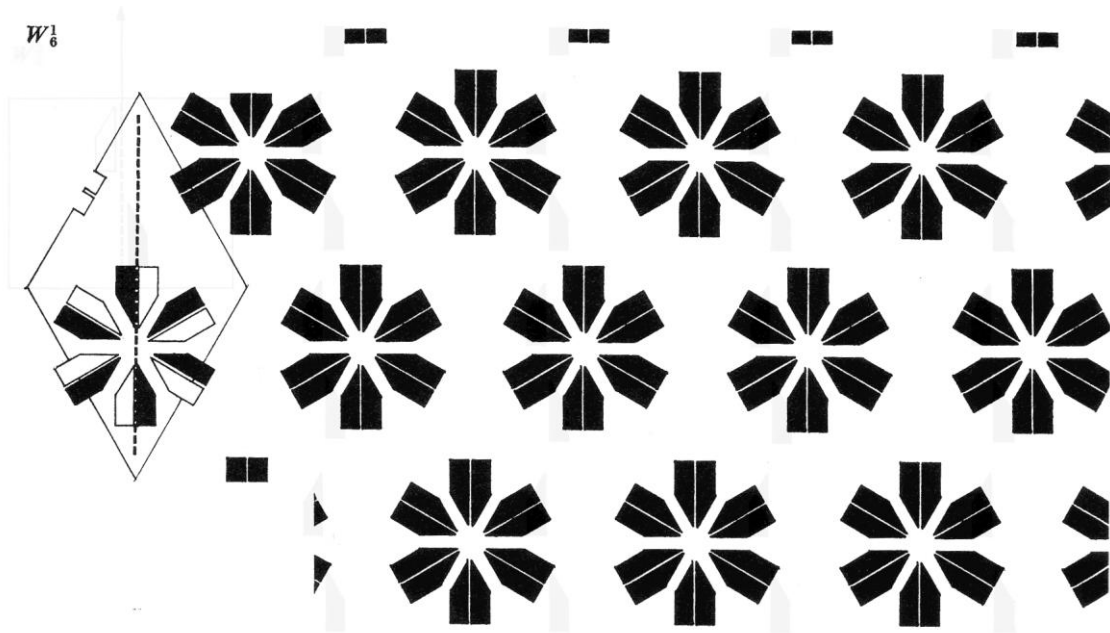


Figure 36. Wallpaper W_6^1 with six point rotations and one direct translation (Steadman and March 1971).

The principle of hexagonal tiling was briefly explored and applied to the wallpaper group concept as presented by Steadman and March (1971). Hexagonal tiling is one of the three regular symmetry group tessellations (triangle, square, and hexagonal) as it

creates three regular hexagons at each mutually incident vertex (Grünbaum and Shephard 1987). Additionally, hexagonal tiling is considered more isotropic than square tiling and has been applied in a cellular automaton (CA) (Gajardo and Goles 1998). Figure 37 depicts a possible application of hexagonal tiling of multiple beehive communes by overlaying the W_6^I wallpaper configuration. Although explored, hexagonal tiling was not incorporated in the final design of the village.

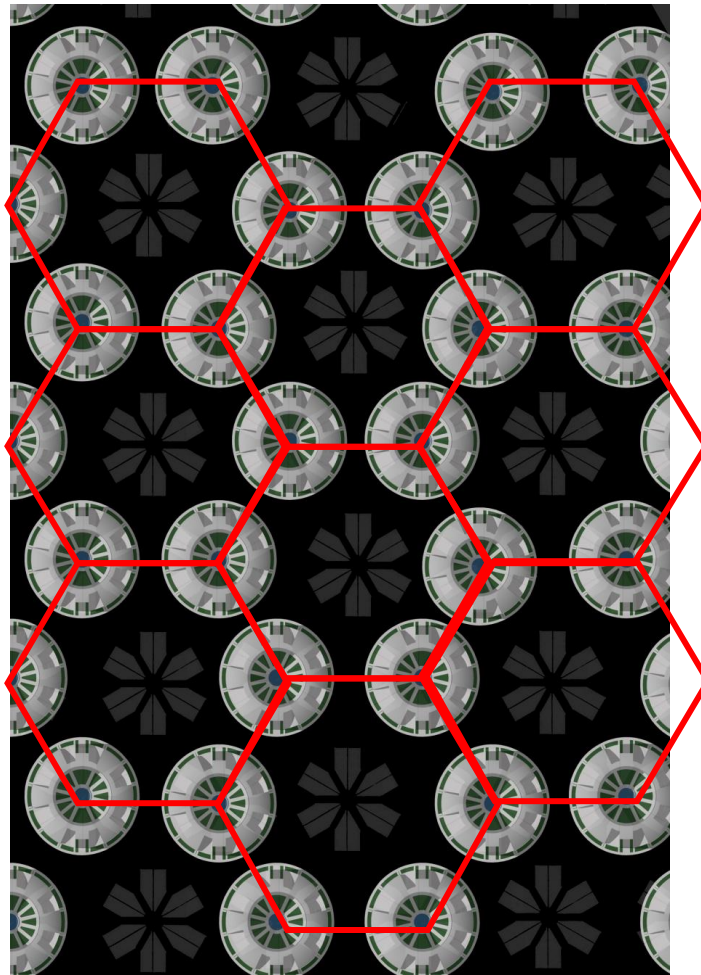


Figure 37. Overlay of hexagonal tiling of beehive communes on the W_6^I wallpaper configuration.

Final Design of the Village

This autonomous village is to be located in South Pretoria, South Africa on the left side of the Ben Schoeman Freeway and bounded by Ashwood Drive and the M10 (figure 38). It was designed to look like a human eye when seen in plan or from an aerial perspective. As mentioned previously, it is designed to house about 2000 people (~500 families). The “beehives” are arranged to form the “brow” of the human eye. Additionally, a development complex (the “eyeball”) will be located in the center of the village and will serve as a main convention center to train residents in various industrial trades. Nearby, there is a wind farm that will provide electricity for supplying hot water to the village.

The final design for the proposed autonomous village layout incorporated an abstraction of the Zulu homestead layout. In the Zulu homestead layout from Kuper (1993), the beehive huts were arranged around the open space (cattle-byre) at the top of the village with the largest of the huts in the center and the smaller ones on either side. As shown in figure 35, the entire village is within the circular open space and the beehive communes are arranged from largest to smallest (left to right) and form the “eyebrow”, while the development center resembles the “eyeball”. As in the Zulu homestead, the village entrance is at the bottom of the layout.

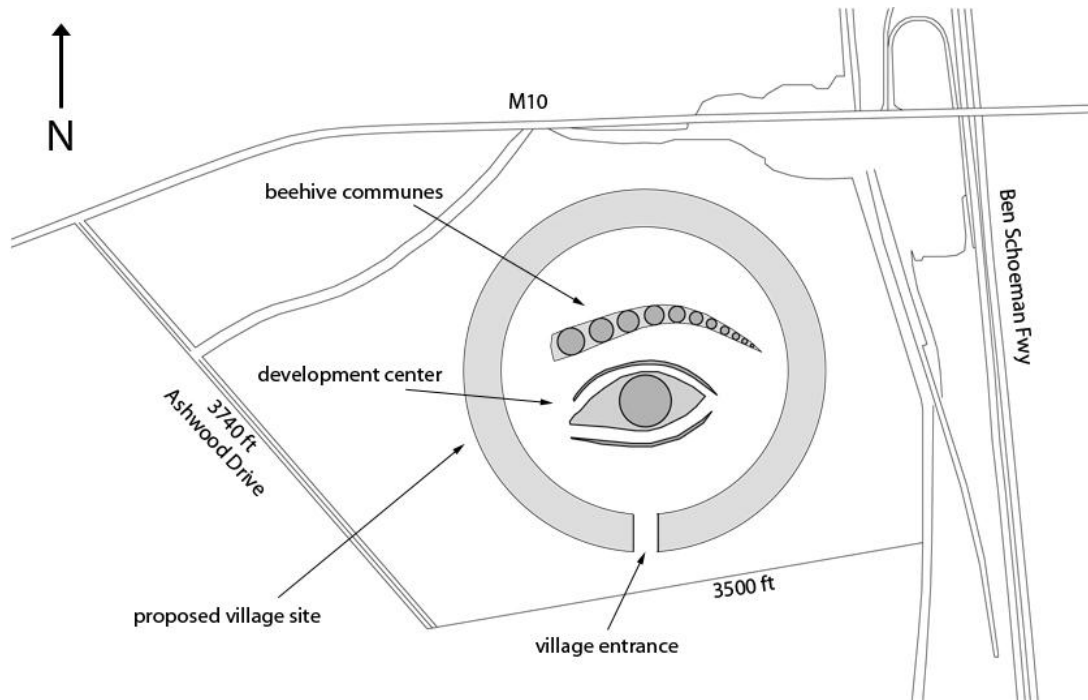


Figure 38. Final layout of the proposed village.

Wind Farm Specifications

As mentioned in the chapter overview, there will be a nearby 2.5 MW wind farm supplying electricity for hot water to the autonomous village. According to EIA (2011), the total United States household electricity consumption in 2009 was approximately 1.36 billion MWh. Water heating only accounted for 127 million MWh (~9.3%) of the total electricity consumption. This translates to approximately 0.41 MWh per person annually. Using these numbers, a ~2000 person village would require about 820 MWh annually. Based on the electricity consumption numbers and assuming 8760 hours in a year, a standard land-based 2.5 MW wind turbine running at maximum efficiency with a capacity factor (CF) of 0.3 can produce ~6570 MWh of energy annually. This suggests that one 2.5 MW wind turbine would be more than sufficient in providing electricity for hot water for the village.

Suggested Distances between the Wind Farm and the Autonomous Village

Based on the results of this work, the wind farm can be placed at any reasonable distance, away from the autonomous village, that will minimize infrastructure costs. It should be noted however that such a conclusion is based on a maximum allowable stress on the tectorial membrane of 120 dB (20 Pa). Future studies should examine the stress level of 85 dB at which point long-term fatigue of the ear may occur. It is currently unknown what long term damage occurs on the tectorial membrane due to both constant noise and low-frequency sounds (infrasound) generated from wind turbines.

REFERENCES

- Adler, H.J., Niemiec, A.J., Moody, D.B., and Raphael, Y. (1995). Tectorial membrane regeneration in acoustically damaged birds: An immunocytochemical technique, *Hearing Research*, 86, 43-46.
- Archer, C.L. and Jacobson, M.Z. (2005). Evaluation of global wind power, *Journal of Geophysical Research*, 110, 1-20.
- British Wind Energy Association (BWEA) (2000). Noise from wind turbines, BWEA: Are wind turbines noisy?, 1-4.
- Beér, J.M. (2009). Higher Efficiency Power Generation Reduces Emissions, National Coal Council, 1-9.
- Bohm, M.C., Herzog, H.J., Parsons, J.E., and Sekar, R.C. (2007). Capture-ready coal plants-options, technologies and economics, *International Journal of Greenhouse Gas Control*, 1, 113-120.
- Byars, E.F., and Snyder, R.D. (1969). *Engineering Mechanics of Deformable Bodies*, 2nd edition, International Textbook Company, Scranton, Pennsylvania.
- Canadian Architecture Collection, McGill University (2001). "Habitat '67 – Planning and Architecture Drawings." The Moshe Safdie Hypermedia Archive, <<http://cac.mcgill.ca>> (February 20, 2011).
- Charron, S. and Botte, M. C. (1988). Frequency selectivity in loudness adaptation and auditory fatigue, *Journal of the Acoustical Society of America*, 83(1), 178-187.
- Colby, W.D., Dobie, R., Leventhall, G., Lipscomb, D., McChunney, R., Seilo, M., and Søndergaard, B. (2009). Wind Turbine Sound and Health Effects: An Expert Panel Review, American Wind Energy Association (AWEA) and Canadian Wind Energy Association (CWEA), 1-85.
- Cotanche, D.A. (1992). Video-Enhanced DIC Images of the Noise-Damaged and Regenerated Chick Tectorial Membrane, *Experimental Neurology*, 115, 23-26.
- Cotanche, D.A. (1999). Structural Recovery from Sound and Aminoglycoside Damage in the Avian Cochlea, *Audiology & Neurotology*, 4, 271-285.
- Dahan E. and Mendelson H. (2001) An Extreme-Value Model of Concept Testing, *Management Science*, 47(1), 106-110.
- Ding-Pfennigdorff, D., Smolders, J.W., Muller, M., and Klinke, R. (1998). Hair cell loss and regeneration after severe acoustic overstimulation in the adult pigeon, *Hearing Research*, 120, 109-120.

- Davis, H. (1965). A model for transduction action in the cochlea, Cold Spring Harbor Symposia on Quantitative Biology, 30, 181-190.
- Economou, A. (1999). The symmetry lessons from Froebel building gifts, Environmental and Planning B: Planning and Design, 26, 75-90.
- Economou, A. and Baker, J. (2006). Kindergarten Revisited, Architectonics.
- Energy Information Administration (EIA) (2008). International Energy Outlook 2008, United States Department of Energy, Washington, DC, 1-250.
- Energy Information Administration (EIA) (2011). "U.S. Residential Electricity Consumption by End Use, 2009." EIA-Independent Statistics and Analysis, <<http://www.eia.doe.gov>> (March 10, 2011).
- Gajardo, A. and Goles, E. (1998). Universal Cellular Automaton over a Hexagonal Tiling with 3 States, International Journal of Algebra and Computation, 11(3), 335-354.
- Gavara, N. and Chadwick, R.S. (2009). Collagen-Based Mechanical Anisotropy of the Tectorial Membrane: Implications for Inter-Row Coupling of Outer Hair Cell Bundles, Public Library of Science (PLoS) One, 4(3), e4877, 1-9.
- Geisler, C.D. and Sang, C. (1995). A cochlear model using feed-forward outer-hair-cell forces, Hearing Research, 86,132-146.
- Ghaffari, R., Aranyosi, A.J., and Freeman, D.M. (2007). Longitudinally propagating traveling waves of the mammalian tectorial membrane, Proceedings of the National Academy of Sciences (PNAS), 104(42), 16510-16515.
- Ghaffari, R., Aranyosi, A.J., Richardson, G.P., and Freeman, D.M. (2010). Tectorial membrane travelling waves underlie abnormal hearing in Tectb mutant mice, Nature Communications, 1(96), 1-6.
- Greb, S., Eble, C., Peters, D., and Rapp, A. (2006). Coal and the Environment, American Geological Institute, Alexandria, VA.
- Grunbaum, B. and Shephard, G.C. (1987). Tilings and Patterns, W.H. Freeman, New York.
- Gu, J.W., Hemmert, W., Freeman, D., and Aranyosi, A.J. (2008). Frequency-Dependent Shear Impedance of the Tectorial Membrane, Biophysical Journal, 95, 2529-2538.

- Gueta, R., Barlam, D., Shneck, R.Z., and Rousso, I. (2006). Measurement of the mechanical properties of isolated tectorial membrane using atomic force microscopy, *Proceedings of the National Academy of Sciences (PNAS)*, 103(40), 14790-14795.
- Gueta, R., Barlam, D., Shneck, R.Z., and Rousso, I. (2008). Sound-Evoked Deflections of Outer Hair Cell Stereocilia Arise from Tectorial Membrane Anisotropy, *Biophysical Journal*, 94, 4570-4576.
- Huskey, A. (2006). International Electrotechnical Commission Standard IEC 61400-11 and Other Procedures: Acoustic Noise Measurement Techniques, Wind Power 2006, Pittsburgh, PA, 1-13.
- International Electrotechnical Commission (IEC) (2002). Wind turbine generator systems-Part 11: Acoustic noise measurement techniques, International Standard IEC 61400-11 (Second Edition), Geneva, Switzerland, 1-46.
- Jung, S.S., Cheung, W-S., Cheong, C., and Shin, S-H. (2008). Experimental Identification of Acoustic Emission Characteristics of Large Wind Turbines with Emphasis on Infrasound and Low-Frequency Noise, *Journal of the Korean Physical Society*, 53(4), 1897-1905.
- Keith, S.E., Michaud, D.S., and Bly, S.H.P. (2008). A proposal for evaluating the potential health effects of wind turbine noise for projects under the Canadian Environmental Assessment Act, *Journal of Low Frequency Noise, Vibration and Active Control*, 27(4), 253-265.
- Kolling, S., Du Bois, P.A., and Benson, D.J. (2005). "A Simplified Rubber Model with Damage." *Crash II, LS-DYNA Anwenderforum, Bamberg*, 1-10.
- Kuper, A. (1993). The 'House' and Zulu Political Structure in the Nineteenth Century, *The Journal of African History*, 34(3), 469-487.
- Kurian, R., Krupp, N.L., and Saunders, J.C. (2003). Tip link loss and recovery on chick short hair cells following intense exposure to sound, *Hearing Research*, 181, 40-50.
- Kurokawa, K. (1977). *Metabolism in Architecture*, Westview Press, Boulder, CO.
- Lamancusa, J.S. (2009). "Outdoor Sound Propagation". < <http://www.mne.psu.edu/lamancusa/me458/>> (April 20, 2011).
- Lawson, R.M. and Richards, J. (2010). Modular design for high-rise buildings, *Proceedings of the Institution of Civil Engineers (ICE): Structures and Buildings* 163, SB3, 151-164.

- Lindley, P.B. (1966). "The Stiffness of Rubber Springs." Proceedings of a Conference held at Imperial College of Science and Technology: Use of Rubber in Engineering, National Rubber Producers' Research Association, London, 1.
- Lu, X., McElroy, M., and Kiviluoma, J. (2009). Global potential for wind-generated electricity, Proceedings of the National Academy of Sciences (PNAS), 106(27), 10933-10938.
- Lukashkin, A.N., Richardson, G.P., and Russell, I.J. (2010). Multiple roles for the tectorial membrane in the active cochlea, Hearing Research, 266, 26-35.
- Martínez, E., Sanz, F., Pellegrini S., Jimenez, E. and Blanco, J. (2009). Life cycle assessment of a multi-megawatt wind turbine, Renewable Energy, 34, 667-673.
- Masaki, K., Weiss, T.F., and Freeman, D.M. (2006). Poroelastic Bulk Properties of the Tectorial Membrane Measured with Osmotic Stress, Biophysical Journal, 91, 2356-2370.
- Makarewicz, R. (2011). Is a wind turbine a point source?, Journal of the Acoustical Society of America, 129(2), 579-581.
- Massachusetts Institute of Technology (MIT) (2007). The Future of Coal: Options for a Carbon-Constrained World, 1-175.
- Meaud, J. and Grosh K. (2010). The effect of tectorial membrane and basilar membrane longitudinal coupling in cochlear mechanics, Journal of the Acoustical Society of America, 127(3), 1411-1421.
- Musial, W., Butterfield, S., and Ram, B. (2006). Energy from Offshore Wind, National Renewable Energy Laboratory (NREL), 1-14.
- National Institute on Deafness and Other Communication Disorders (NIDCD) (2008). NIDCD Fact Sheet: Noise-Induced Hearing Loss, Bethesda, Maryland.
- Pederson, E., van den Berg, F., Bakker, R., and Bouma, J. (2009). Response to noise from modern wind farms in The Netherlands, Journal of the Acoustical Society of America, 126(2), 634-643.
- Phillips, M. (2003). Genetics of Hearing Loss, MEDSURG Nursing, 12(6), 386-390, 411.
- Poje, C.P., Sewell, D.A., Saunders, J.C. (1995). The effects of exposure to intense sound on the DC endocochlear potential in the chick, Hearing Research, 82, 197-204.
- Richter, C.P., Emadi, G., Getnick, G., Quesnel, A., and Dallos, P. (2007). Tectorial Membrane Stiffness Gradients, Biophysical Journal, 93, 2265-2276.

- Richardson, G.P., Lukashkin, A.N., and Russell, I.J. (2008). The tectorial membrane: One slice of a complex cochlear sandwich, *Current Opinion in Otolaryngology & Head and Neck Surgery*, 16(5), 458-464.
- Ross, M. (1978). *Beyond Metabolism: New Japanese Architecture*, McGraw-Hill, New York.
- Ryan, A (2000). Protection of auditory receptors and neurons: Evidence for interactive damage, *Proceedings of the National Academy of Sciences (PNAS)*, 97(13), 6939-6940.
- Salt, A.N. (2010). "Infrasound: Your ears 'hear' it but they don't tell your brain", *Symposium on Adverse Health Effects of Industrial Wind Turbines*, Ontario, Canada, 1-30.
- Salt, A.N. and Hullar, T.E. (2010). Responses of the ear to low frequency sounds, infrasound and wind turbines, *Hearing Research*, 268, 12-21.
- Schmal, P.C., Visscher, J., Flagge, I., and Kurokawa, K. (2005). *Kisho Kurokawa: Metabolism and Symbiosis*, Jovis, Berlin.
- Shoelson, B., Dimitriadis, E.K., Cai, H., Kachar, B., and Chadwick R.S. (2004). Evidence and implications of inhomogeneity in tectorial membrane elasticity, *Biophysical Journal*, 87(4), 2768-2777.
- Steadman, P. and March, L. (1971). *The Geometry of Environment*, MIT Press, Cambridge, MA.
- Stiny, G. (1980). Kindergarten grammars: designing with Froebel's building gifts, *Environment and Planning B: Planning and Design*, 7, 409-462.
- Thresher, R., Robinson, M., and Veers, P. (2008). *The Future of Wind Energy Technology in the United States*, National Renewable Energy Laboratory (NREL), 1-12.
- Truax, B. (1999). *Handbook for Acoustic Ecology*, 2nd Edition, Cambridge Street Publishing, Burnaby, BC.
- van den Berg, G.P. (2003). Effects of the wind profile at night on wind turbine sound, *Journal of Sound and Vibration*, 277, 955-970.
- van den Berg, G.P. (2006). *The sound of high winds: the effect of atmospheric stability on wind turbine sound and microphone noise*, PhD Dissertation, University of Groningen, Netherlands.

Vale, B. and Vale, R. (2000). *The New Autonomous House*, Thames and Hudson, London, UK.

Wang, B., Lu, H., and Kim, G. (2002). A damage model for the fatigue life of elastomeric materials, *Mechanics of Materials*, 34, 475-483.